Fabrication of a Nanoscale Magnesium/Copper Metal−Organic Framework on Zn-Based Guided Bone Generation Membranes for Enhancing Osteogenesis, Angiogenesis, and Bacteriostasis Properties

Kai Chen, Yifan Wang, Hongyan Tang, Xufeng Niu, Hongtao Yang, Yanjie Bai, Xuenan Gu,* and Yufeng Zheng*

Read Online

ACCESS | Metrics & More | Article Recommendations | Supporting Information

ABSTRACT: Recently, zinc (Zn) and its alloys have demonstrated great potential as guided bone regeneration (GBR) membranes to treat the problems of insufficient alveolar bone volume and long-term osseointegration instability during dental implantology. However, bone regeneration is a complex process consisting of osteogenesis, angiogenesis, and antibacterial function. For now, the in vivo osteogenic performance and antibacterial activity of pure Zn are inadequate, and thus fabricating a platform to endow Zn membranes with multifunctions may be essential to address these issues. In this study, various bimetallic magnesium/copper metal−organic framework (Mg/Cu-MOF) coatings were fabricated and immobilized on pure Zn. The results indicated that the degradation rate and water stability of Mg/Cu-MOF coatings could be regulated by controlling the feeding ratio of Cu^{2+}. As the coating and Zn substrate degraded, an alkaline microenvironment enriched with Zn^{2+}, Mg^{2+}, and Cu^{2+} was generated. It significantly improved calcium phosphate deposition, differentiation of osteoblasts, and vascularization of endothelial cells in the extracts. Among them, Mg/Cu1 showed the best comprehensive performance. The superior antibacterial activity of Mg/Cu1 was demonstrated in vitro and in vivo, which indicated significantly enhanced bacteriostatic activity against Gram-positive *Staphylococcus aureus* and Gram-negative *Escherichia coli* as compared to that of the bare sample. Bimetallic Mg/Cu-MOF coating could properly coordinate the multifunction on a Zn membrane and could be a promising platform for promoting its bone regeneration, which could pave the way for Zn-based materials to be used as barrier membranes in oral clinical trials.

KEYWORDS: *zinc, Mg/Cu-MOF, guided bone regeneration (GBR), osteogenesis, angiogenesis, bacteriostasis activity*
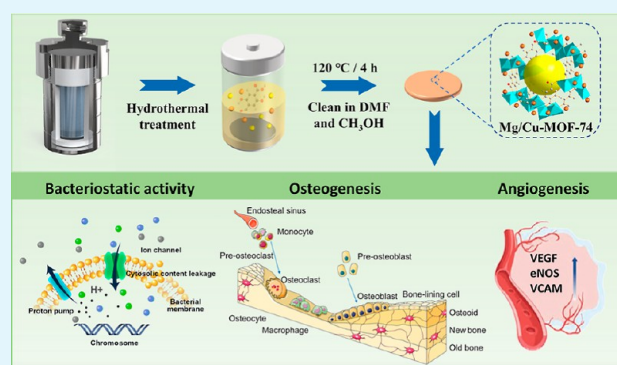
1. INTRODUCTION

Guided bone regeneration (GBR) is a well-established technique used for augmentation of deficient alveolar ridges.[1] It employs a barrier membrane to occlude soft-tissue cells and maintain a secluded space for slow-growing osteoblasts to repopulate the defect, ultimately achieving the goal of bone augmentation.[2−4] Successful GBR relies on the development and maintenance of space for the ingrowth of bones, osteoblast differentiation, angiogenesis to provide the required blood supply, and antimicrobial properties. Adequate membrane selection is consequently critical for GBR.[5−7] Commercially available membranes are categorized as either nonresorbable or resorbable materials. As typical nonresorbable membranes, the expanded polytetrafluoroethylene (ePTFE) membranes and titanium mesh are considered the standard reference for GBR because of their exceptional space-making capacity and controlled barrier function. However, this type of membrane requires additional surgery for removal. They also have a

higher risk to be exposed to the oral environment, which is usually associated with subsequent infection and diminished bone growth.[8] Resorbable collagen membranes have been developed to avoid a secondary surgery, despite their inherent lack of mechanical stability, especially when they are used for vertical augmentation.[2,4] This, hence, encourages us to be still dedicated to optimizing the membrane materials by addressing sufficient mechanical properties and biodegradability, as well as inhibiting various bacterial infections and favoring angiogenesis and osteogenesis in the bone defect.

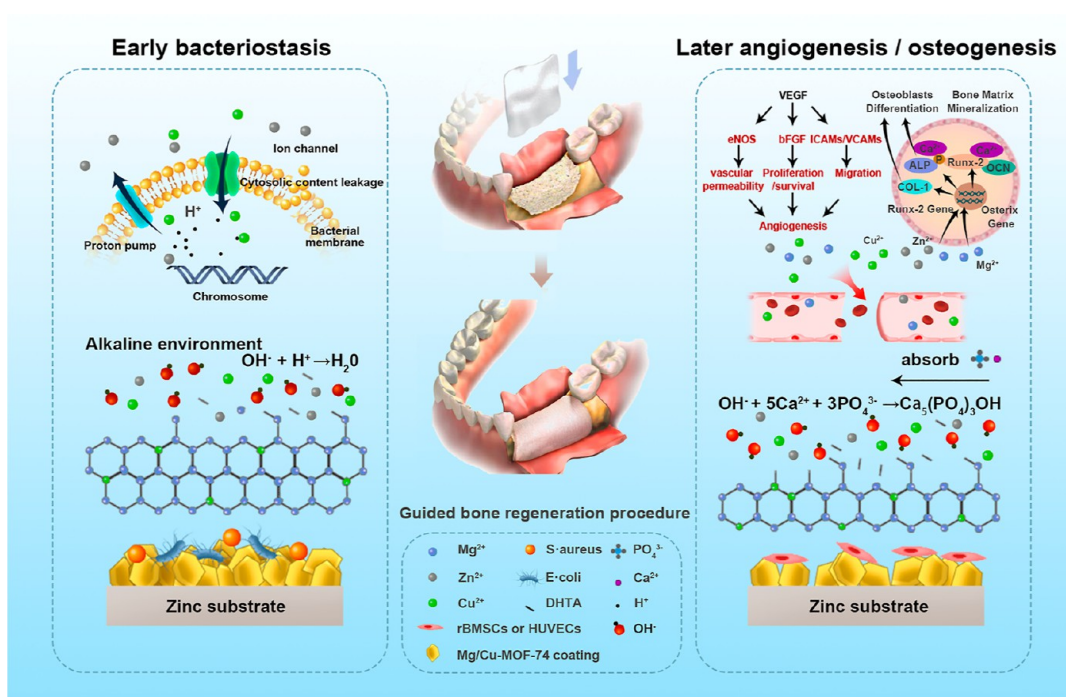**Scheme 1. Schematic Representation of the Biological Effects of a Mg/Cu-MOF-Coated Zn Membrane and Its Potential Therapeutic Effect in the GBR Procedure**

Zn and Zn alloys have been suggested as potential candidates for GBR membranes recently.[9−11] Zn is mechanically stronger than polymers while maintaining comparable ductility. The tensile strength and elongation of extruded pure Zn are ∼166 MPa and ∼40%, respectively.[11] Zn exhibits an appropriate degradation rate in the physiological environment, displaying osteogenic activity and antibacterial properties due to Zn^{2+} leaching during their degradation.[12,13] However, the pure Zn membranes failed to outperform pure Ti counterparts in bone formation and ingrowth in a rabbit cranial defect model,[10] and the osteogenic activity of pure Zn membranes should be optimized. Besides, previous studies have also confirmed that the osteogenic and antibacterial activity of pure Zn implants are grossly inadequate.[11,12] Until now, Zn-based alloys are still facing some challenges to serve as a platform in GBR because the antibacterial effects of Zn^{2+} have been mostly explained by dosage-dependent cytotoxicity.[14] It implies that the therapeutic window for Zn^{2+} favoring osteogenesis could exhibit limited antibacterial effects, which was also confirmed in other research works.[9,12,15] Even though the degradation of Zn-based materials and Zn^{2+} leaching kinetics can be precisely controlled, it is still difficult to balance their antibacterial, osteogenic, and angiogenic effects only relying on single Zn^{2+} for GBR application.

Metallic ions are commonly utilized to modify the Ti surface owing to their superior capacity to stimulate biological functions and cost effectiveness. For instance, magnesium (Mg) is a common ingredient in bones and its osteoinductive potential has been extensively reported.[16,17] Yu et al. indicated that Zn and Mg ions have synergistic effects in enhancing adhesion ability and osteogenic differentiation of rBMSCs.[18] Dual Zn/Mg-ion-implanted Ti can simultaneously increase the osteogenesis-related gene expressions (*RunX2*, *OCN*, and *ALP*) and have a certain inhibitory effect on the growth of oral anaerobic bacteria.[18] Copper (Cu) has been well

documented to have antibacterial properties. Zn^{2+} has synergism with Cu^{2+} in destroying bacterial membranes, leading to obvious antibacterial activity at low levels of Zn^{2+} and Cu^{2+} and circumventing the cytotoxicity caused by high-ion concentrations.[19] Significantly improved and balanced antibacterial and osteogenic activities were also achieved for Cu/Zn-co-doped PCL membranes.[20] Besides, the release of Cu^{2+} from coatings can effectively reduce the risks of oral infections due to premature membrane exposure. Cu^{2+} has the potential to limit collagen fibril production while increasing angiogenesis, hence accelerating blood vessel infiltration into the bone defect and facilitating future bone regeneration.[21,22]

Techniques of plasma immersion ion implantation, magnetron sputtering, and microarc oxidation are commonly used to fabricate metal-ion-loaded metallic biomaterials. However, these techniques require complex and skill-intensive processing steps and expensive equipment. Metal−organic frameworks (MOFs), constructed by the periodic coordination of metallic ions and organic ligands,[23] can afford as metal ions carrier and achieve certain ion release through the degradation of MOFs. A recent study fabricated Ce/Sr dual-loaded MOF coatings on a Ti surface through coordination between *p*-xylylenebisphosphonate (PXBP) and Ce/Sr ions. Benefiting from Ce and Sr ion release, the Ce/Sr-MOF-coated Ti activated the AMP-activated protein kinase (AMPK) signaling pathway in mesenchymal stem cells (MSCs), reducing the ROS levels and ultimately achieving the goal of alleviating osteoporosis.[24] Therefore, the feasibility of an MOF as a multiple metal ion carrier can be conceived, and we hypothesized that constructing Mg/Cu-MOF coatings on Zn offered a minimalist approach to improve biological activities of Zn-based membranes via multiple metal ion release.

In this study, to optimize the biological properties of pure Zn membranes, hybrid Mg/Cu-MOF coatings were prepared on Zn membranes to synergistically achieve antibacterial,
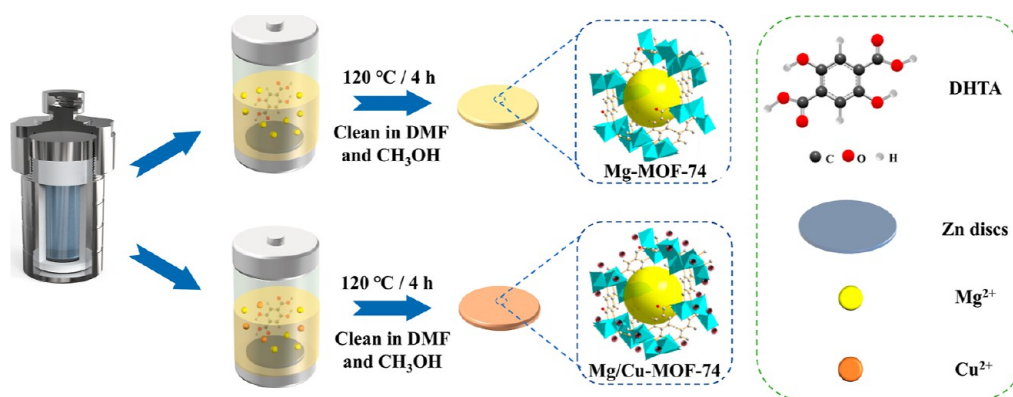
Figure 1. Schematic diagram of synthesizing Mg-MOF-74 and bimetallic Mg/Cu-MOF coatings on pure Zn discs.

osteogenic, and angiogenic properties, as displayed in Scheme 1. A Mg-based MOF (Mg-MOF) was selected considering the excellent biosafety on account of the osteogenesis effect of Mg and high in vivo clearance efficiency.[25,26] Mg-MOF coating can supply Mg^{2+} during coating degradation, and the fabrication process of the Mg-MOF coating is convenient. Doping Cu^{2+} in Mg-MOF could further improve the water stability.[27] Mg/Cu-MOF coating doped with different Cu^{2+} ratios was designed and constructed on Zn-based membranes through a facile one-step hydrothermal method. To verify the multifunctionality of fabricated membranes, the degradation behavior, the in vitro and in vivo antibacterial activity, and osteogenesis and angiogenesis in vitro were systematically investigated. This study could provide valuable information for exploring the MOF application on the surface modification of Zn-based materials and offer a facile strategy to promote the bone regeneration of Zn-based membranes in the GBR procedure.

2. EXPERIMENTAL SECTION

2.1. Materials Preparation. In this study, pure Zn discs (99.99 wt %) with a size of ϕ 10 × 1 mm and pure Zn foils (99.99 wt %, 20 × 10 × 0.5 mm) were used as raw materials. The discs were cut from the extruded pure Zn bars prepared according to our previous study,[28] and the pure Zn foils were purchased from Goodfellow (Shanghai) Trading Co., Ltd., China. Before experiments, pure Zn discs were ground by abrasive papers to 2000#, followed by cleaning in acetone and ethanol for 5 min each. In addition, N,N-dimethylformamide (DMF, C_3H_7NO) and 2,5-dihydroxy terephthalic acid (DHTA, $C_8H_6O_6$) were obtained from Macklin Reagent Co., Ltd. (Beijing, China). Absolute ethyl alcohol (C_2H_5OH), absolute methanol (CH_3OH), magnesium nitrate hexahydrate ($Mg(NO_3)_2·6H_2O$), and cupric nitrate ($Cu(NO_3)_2·3H_2O$) were purchased from Sinopharm Chemical Reagent Co., Ltd. (Beijing, China). Dulbecco's modified Eagles medium (DMEM), fetal bovine serum (FBS), and TRIzol lysate were derived from Thermo Fisher Co., Ltd. (Gibco, USA). Rhodamine-labeled ghost pen cyclic peptide, 4′,6-diamidino-2-phenylindole (DAPI), 4% paraformaldehyde (PFA), and phosphate-buffered saline (0.01 M, PBS) were acquired from Solarbio Science & Technology Co., Ltd. (Beijing, China).

2.2. Fabrication of Mg/Cu-MOF Coating. According to previous report,[27] the concentration of Cu dopant presents a gradient increase, and the prepared samples were denoted as Mg-MOF, MgCu1, MgCu3, and MgCu5 alloys, as displayed in Table S1. A facile one-step hydrothermal method was adopted to facilitate the growth of Mg/Cu-MOF coatings on Zn discs. According to Table S1, the solute of the reaction solution was weighed, and the compound solvent was prepared according to the DMF/C_2H_5OH/distilled water ratio of 60:6:6 (mL). Subsequently, the solution was evenly mixed on a magnetic mixer (SP88857106, Thermo Fisher, USA). Then, the polished pure Zn discs were placed into the Teflon container in the

reaction kettle, and the mixed reaction solution was added with a ratio of 10 mL/disc. Afterward, the reaction kettle was heated at 120 °C for 4 h in the furnace. As the furnace was cooled to room temperature, the samples were removed from the solution and cleaned with DMF as well as CH_3OH three times. After being cleaned, the samples were dried by an air blower. The corresponding synthesis diagram is shown in Figure 1.

2.3. Characterization of Surface Coating. The surface morphologies and chemical component distributions of different Mg/Cu-MOF coatings were observed by a stereoscopic microscope (Olympus, SZX7, Japan) and a scanning electron microscope (JSM-7001F, Japan) equipped with an energy-diffraction spectrometer (Oxford). To verify the deposition of Mg/Cu-MOF74 coatings, a Fourier transform infrared (FTIR) spectrometer (Excalibur 3100, Varian) was employed to detect the functional group composition of surface coatings. Besides, the phase compositions of different samples were examined by an X-ray diffractometer (D8 Focus, Bruker, Germany) with Cu $K\alpha$ radiation. The scans were carried out in a continuous fashion at 2θ from 5 to 50° with a scan rate of 4°/min. Furthermore, the water contact angles of different samples were measured with a contact angle analyzer (Shanghai Powereach Digital Technology Equipment Co. Ltd., China).

2.4. Coating Adhesion Tests. *2.4.1. Scratch Tests.* The adhesion strength between coatings and the substrate was analyzed and compared by scratch tests. A micro scratch meter (MCT³, Anton Paar, Austria) was used for the scratch experiments. A Rockwell diamond probe with a diameter of 200 μm was used to apply a 0−7 N progressive force at a force loading rate of 0.1 N/min. Then, a 1 mm scratch was created on the surface at an advancing speed of 1 mm/min. During tests, the load curves and penetration depth were both recorded, and the morphologies of scratches were observed by scanning electron microscopy (SEM). Generally, the load which causes the initial rupture of the coating is called the "lower critical load (L_{c1})", whereas the load which causes the coating to completely break away from the substrate is called the "upper critical load (L_{c2})".[29,30] The L_{c2} on each coating was calculated according to the relationship between the load curve and the penetration depth, and it was used to evaluate the bonding strength of the coatings.

2.4.2. U-Bending Deformation Treatment. The Mg/Cu-MOF coatings were also fabricated on the surfaces of pure Zn foils. According to ASTM G 30−97 standard, the pure Zn foils were bent 180° around a predetermined radius (ϕ = 12 mm) to stimulate the actual application scenarios of GBR membrane, as shown in Figure S1. The total strain (ε) on the outside of the strip was about 4.2%. The morphologies of bent foils were examined by SEM to evaluate the cracking resistance of the coating.

2.5. Immersion Tests. To study the degradation profile of Mg/Cu-MOF-coated samples, the immersion tests were carried out in Hank's solution at 37 ± 0.5 °C and lasted for 14 days. The chemical components of Hank's solution can be found in our previous report.[28] The ratio of the immersed solution to sample areas was approximately 20 mL/cm². During the degradation process, the pH value of the

solution was recorded, and the released Zn^{2+}, Mg^{2+}, and Cu^{2+} were also determined by an inductively coupled plasma optical emission spectrometer (Optima 5300DV, USA). After immersion tests, the samples were removed from the solution, gently rinsed by ultrapure water, and dried at room temperature. Afterward, the corrosion morphologies, chemical components of corrosion products, and cross section of samples were analyzed by SEM and energy-dispersive spectrometry (EDS). According to ASTM-G1-03 standard, the corroded samples were soaked in CrO_3 solution (200 g/L) at 80 °C for 1 min and also examined by SEM. Therefore, the corrosion rate of different samples can be calculated as follows

$$CR = 87.4 \times (m_i - m_f)/A\rho t \tag{1}$$

where m_i (mg) is the initial weight of samples before immersion, m_f (mg) is the final weight of samples after chemical cleaning, ρ is the density of samples (g/cm^3), A is the surface areas of sample exposed to solution (cm^2), and t is the immersion time (h).

2.6. Electrochemical Measurement. An electrochemical workstation (Autolab, Metrohm, Switzerland) and a standard three-electrode electrochemical cell were employed to examine the electrochemical behavior of the Mg/Cu-MOF-coated samples in Hank's solution at 37 ± 0.5 °C. The Mg/Cu-MOF-coated samples, saturated calomel electrode (SCE), and platinum electrode were set as working, reference, and counter electrodes, respectively. The effective working areas were about 1 cm^2. Primarily, the stability of the open-circuit potential (OCP) was measured and continuously monitored for 3600 s. Then, electrochemical impedance spectroscopy (EIS) tests were conducted at frequencies ranging from 100 kHz to 0.1 Hz with an alternating current amplitude of 10 mV. Subsequently, the potentiodynamic polarization (PDP) tests were carried out from −0.3 to +0.3 V OCP) at a scan rate of 1 mV/s. Through the Tafel extrapolation method, the corrosion potential (E_{corr}) and corrosion current density (i_{corr}) of samples were obtained. More importantly, on the basis of ASTM-G102-89 standard, the electrochemical corrosion rate (CR$_{PDP}$) of samples can be acquired as follows

$$CR_{PDP} = 3.27 \times 10^{-3} i_{corr} EW/\rho \tag{2}$$

where i_{corr} ($\mu A/cm^2$) is the corrosion current density, EW is the equivalent weight, and ρ is the density of Zn (g/cm^3).

2.7. Cytocompatibility Assay. The mouse osteoblast cell line (MC3T3-E1) and human umbilical vein endothelial cells (HUVECs) were used to evaluate the in vitro biocompatibility of the samples. Both cell types were cultured in DMEM supplemented with 10% FBS, 100 g/mL streptomycin, and 100 g/mL penicillin at 37 ± 0.5 °C in a humidified atmosphere of 5% CO$_2$. The samples were first incubated in DMEM for 72 h, and the supernatants were collected as alloy extracts. The cytocompatibility of samples was indirectly evaluated by diluted alloy extracts (25% and 10%). Briefly, for MC3T3-E1 cells and HUVECs, 3000 cells/well were seeded in 96-well culture plates and incubated for 24 h. Afterward, the culture medium was discarded and replaced with diluted alloy extracts with refreshed DMEM set as the control group. After incubation for 2 or 4 days, the cell viability of MC3T3-E1 and HUVECs was measured by a Cell Counting Kit-8 (CCK-8, Dojindo, Japan) protocol. The absorbance of each well at 450 nm was read by a microplate reader (Varioskan LUX, Thermo Fisher, US). More importantly, the cell viability can be obtained as follows

$$\text{cell viability} = \frac{OD_{test} - OD_{blank}}{OD_{control} - OD_{blank}} \tag{3}$$

where OD_{test}, OD_{blank}, and $OD_{control}$ are the mean absorbance values of the test, blank, and control groups, respectively. Moreover, the concentrations of Mg^{2+}, Zn^{2+}, and Cu^{2+} in the extracts were also measured by inductively coupled plasma−optical emission spectrometry (ICP−OES).

Furthermore, the morphologies of MC3T3-E1 cells and HUVECs were characterized by nucleus staining and cytoskeleton staining methods. In brief, after 4 days of incubation, the diluted extracts were removed, and the cells were gently rinsed by PBS three times.

Following that, the cells were fixed by 4% paraformaldehyde solution for 1 h and permeabilized in 0.1% Triton X-100 for 8 min at room temperature. Then, the cells were stained with the rhodamine-labeled ghost pen cyclic peptide and cultured in the dark for 30 min. Finally, the cells were incubated in DAPI solution for 30 s. The morphologies, amount, and distribution of cells were photographed by an inverted fluorescence microscope (IX71, Olympus, Japan).

2.8. Alkaline Phosphatase Activity. The osteogenic differentiation performance of different samples was examined by the alkaline phosphatase (ALP) activity of MC3T3-E1 cells. In brief, the MC3T3-E1 cells were seeded in a 6-well plate with a density of 2×10^4 cells/well. After the mixture was incubated for 24 h, the medium was removed and replaced with 25% diluted extracts. After incubation for 3 or 7 days, the medium was discarded, and the cells were gently rinsed by PBS three times. Then, the ALP activity of MC3T3-E1 cells was measured by an ALP Quantitative Assay Kit (Beyotime Biotechnology, China). Besides, the total protein concentration of cells was determined by a BCA Protein Assay Kit (Solarbio, Beijing), and the ALP concentration was normalized.

2.9. Expression of Osteogenic and Vascularization Genes. The expression of both osteogenic genes (*Col-1*, *Runx-2*, *ALP*, and *OCN*) in MC3T3-E1 cells and vascularization genes (*e-NOs*, *VEGF*, and *VCAM-1*) in HUVECs was measured by real-time reverse-transcription quantitative polymerase chain reaction (RT-qPCR). At first, two types of cells were seeded in 6-well plates at a density of 2×10^4 cells/well and cultured overnight. Then, the culture medium was replaced with 25% diluted extracts and incubated for 3 or 7 days. The cells cultured by DMEM were set as the control group. After culture, the cells were gently rinsed by PBS, and 0.1% TRIzol reagent (Invitrogen, USA) was utilized to extract RNA according to the manufacturer's instructions. Following that, 1.5 μg of RNA was used for reverse transcription and cDNA synthesis by the Prime Script RT Reagent Kit (Takara, Japan), and RT-qPCR was performed in quadruplicate using SYBR Premix Ex *Taq*II (Takara, Japan) with a real-time PCR detection system (Bio-Rad Laboratories GmbH, Munich, Germany) and iQ5Manager software. The primer sequences of osteogenic genes and vascularization genes are shown in Table S2.

2.10. Cell Migration and Nitric Oxide Release. HUVECs were seeded in 6-well plates with a density of 1.5×10^6 cells/well and cultured for 24 h to allow cell attachment. Then, a scratch was made in each well by a sterile spearhead, and each well was gently rinsed with PBS two times. Afterward, 2.5 mL of 25% diluted extracts containing 2% FBS was added to each well. After 0, 6, 12, and 24 h of incubation, the migration of cells on both sides of the scratch was observed by an IX71 optical microscope. More importantly, the residual scratch areas were quantitatively analyzed by the Image-Pro Plus 6.0 software, and the cell migration rate can be obtained as follows

$$\text{cell migration rate} = \frac{area_0 - area_t}{area_0} \times 100\% \tag{4}$$

where $area_0$ and $area_t$ represent the residual scratch areas at 0 h and at different target times (t h), respectively.

Furthermore, during the cell migration tests, the supernatants of the cell culture medium were collected at different time intervals. Nitric oxide (NO) release, an important factor that the HUVECs are released into the medium, was quantified according to the protocol of Griess Reagent Assay Kit (Beyotime Biotechnology, China).

2.11. In Vitro Antibacterial Behavior. To measure the antibacterial performance of the alloys, Gram-positive *Staphylococcus aureus* (*S. aureus*, ATCC 29213) and Gram-negative *Escherichia coli* (*E. coli*, ATCC 35218) were both utilized. Briefly, the bacterial suspension was cultured in tryptone soy broth (TSB), and the concentration of bacterial strains was adjusted to about 10^6 CFU/mL according to our previous report.[8] Before tests, the alloys were disinfected for 30 min with 75% absolute ethyl alcohol and rinsed with PBS three times. Besides, the Ti-6Al-4V alloy was set as the control group. Afterward, the alloys were placed in a 24-well plate, and 1 mL of bacterial suspension was added in each well. Then, the plate was cultured in the shaker incubator for 24 h at 37 °C in a
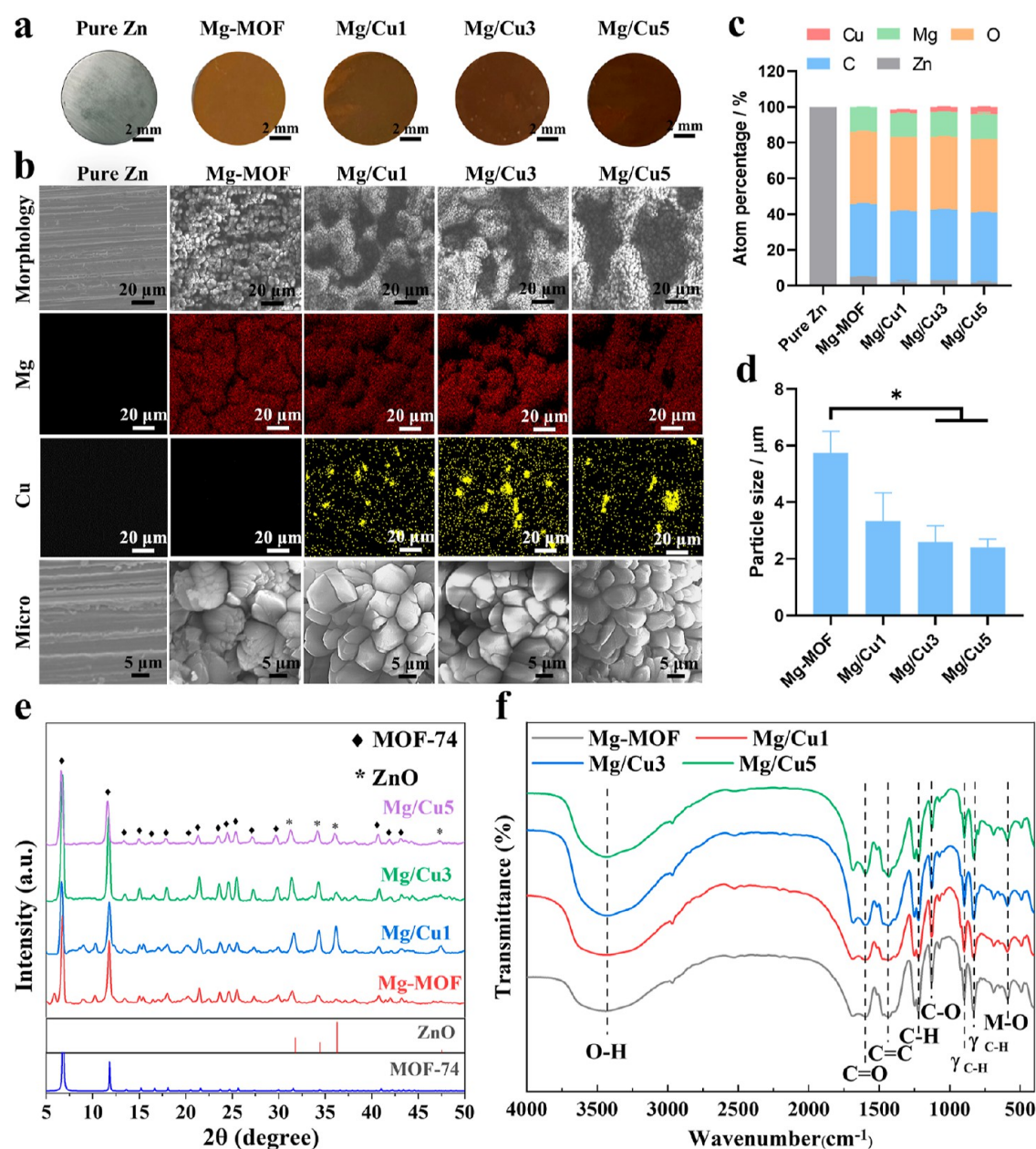
Figure 2. (a) Macromorphologies of pure Zn and Mg/Cu-MOF-coated samples, (b) morphologies and elemental mapping results of surface coating formed on pure Zn, Mg-MOF, Mg/Cu1, Mg/Cu3, and Mg/Cu5 alloy surfaces (the fourth line shows a higher magnification of coating morphologies), (c) EDS results of surface layers, (d) particle size of various Mg/Cu-MOF coatings, (e) XRD diffraction patterns, and (f) FTIR patterns of various Mg/Cu-MOF coatings on the pure Zn surface. *$P < 0.05$.

humidified atmosphere with 5% CO_2. After culture, the bacterial suspension was collected and further diluted by 100-fold. The 100-fold-diluted bacterial suspension was spread on the agar plates and cultured again for 24 h. The distribution of bacterial colonies was then photographed, and their number was analyzed by ImageJ software. Therefore, the antibacterial rate (AR) of the alloys can be obtained by the following equation

$$AR = \frac{N_{control} - N_{sample}}{N_{control}} \quad (5)$$

where $N_{control}$ and N_{sample} denote the number of bacterial colonies in the control and test groups, respectively. Each group's antibacterial performance was repeated at least three times. Besides that, the concentrations of proteins in the suspended bacteria cocultured with the materials were determined by a BCA Protein Assay Kit (Solarbio, Beijing).

2.12. Mouse Subcutaneous Infection Model. To test the in vivo bacteriostatic activity of MOF-coated samples, *S. aureus* *S. aureus*, ATCC 29213) and a mouse subcutaneous infection model were used. All animal operations and research were authorized by the Animal Ethics Committee of the School of Biological Science and Medical Engineering affiliated with Beihang University. Eighteen male Sprague−Dawley rats (200−220 g) were provided by the Department of Laboratory Animal Science, Peking University Health Science Center, Beijing, China. According to the biocompatibility and bacteriostasis results in vitro, three groups were further evaluated in vivo, including control (Ti-6Al-4 V), pure Zn, and Mg/Cu1 groups. The rats were sedated prior to surgery with intraperitoneal doses of ketamine (10 mg·kg^{-1}) and 2% xylazine (5 mg·kg^{-1}). The fur on the rats' dorsal sides was shaved and treated with iodine. Following that, a longitudinal incision was made, and samples from various groups (ϕ 10 × 1 mm) were implanted into the subcutaneous pocket. Notably, the implanted samples were precultured in *S. aureus* suspension for 5
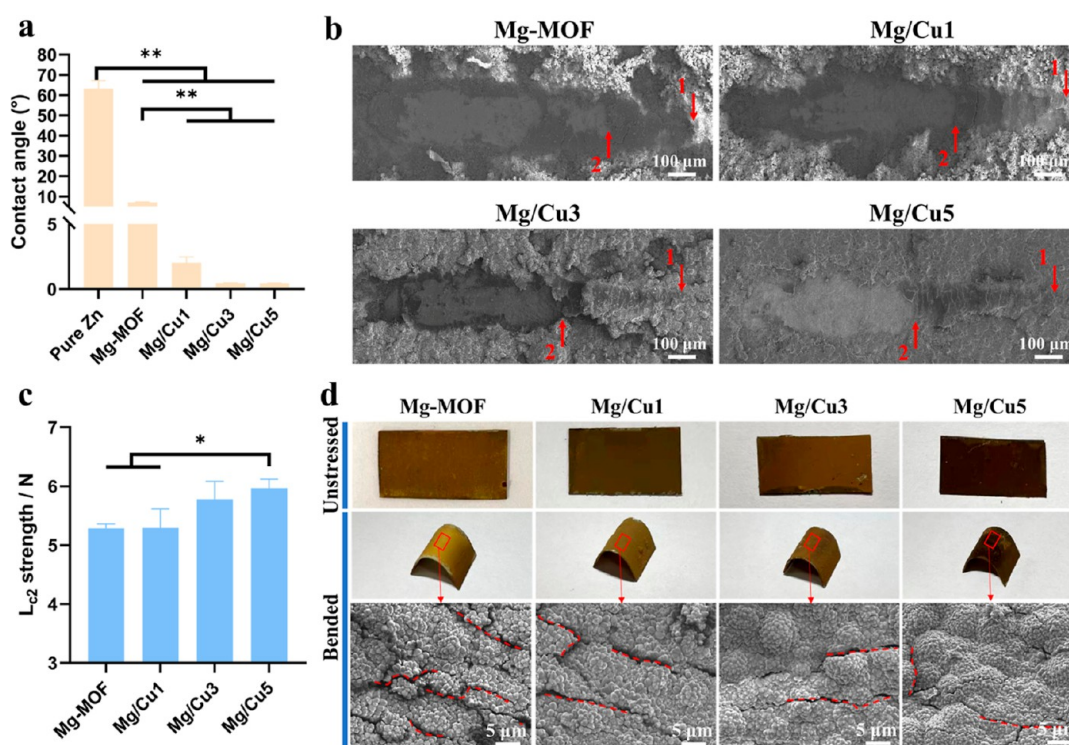
Figure 3. (a) Water contact angle values of pure Zn and Mg/Cu-MOF-coated samples, (b) SEM pictures illustrating the coating morphologies after scratch tests (locations 1 and 2 indicate L_{c1} and L_{c2}, respectively), (c) adhesion strength of Mg/Cu-MOF coating on the Zn substrate, as indicated by L_{c2} in scratch tests, and (d) macro- and micromorphologies of unstressed and bent strips with Mg/Cu-MOF coatings (red dotted lines indicate the formation of microcracks). *$P < 0.05$, **$P < 0.01$.

min and then 100 μL volume of *S. aureus* suspension was simultaneously administered into the subcutaneous pocket. Suture lines were then used to seal the incisions on the dorsal side. The rats were sacrificed, and the implanted samples were obtained after 5 and 10 days of in vivo infection. Following that, the obtained samples were soaked in PBS and ultrasonically oscillated for 5 min. The bacteria were then collected, diluted, and spread on an agar plate. After 24 h of incubation, the morphology of bacteria was recorded, and the antibacterial rate was determined using ImageJ software (eq 5).

Additionally, the tissues around the samples were collected, fixed with 4% paraformaldehyde, dried with gradient alcohol solutions, and embedded in poly(methyl methacrylate) (PMMA). The mounted tissues were sliced to a thickness of 50 μm with a diamond saw (Leica SM2500E, Germany) to obtain histological sections. The obtained slices were then stained with hematoxylin and eosin (H&E) and Masson's trichrome before being examined by an optical microscope (IX71, Olympus, Japan).

2.13. Statistical Analysis. SPSS 21.0 software (SPSS Inc., Chicago, IL, USA) was used to conduct statistical analysis. The differences between groups were analyzed by the one-way analysis of variance (ANOVA) method. Each experiment was repeated at least three times, and all data were expressed as mean $\pm$ standard deviation.

3. RESULTS AND DISCUSSION

3.1. Surface and Interface Characterization. Figure 2a,b shows the macro- and micro-morphologies of pure Zn and Mg/Cu-MOF-coated samples. In Figure 2a, it can be observed that the surface morphology changes from a bright white color for pure Zn to yellowish-brown color for Mg/Cu5 samples. The coating morphologies present granular layers with a microsize, which is consistent with the previous study reported by Campbell and Tokay.[31] As the Cu addition increases, the brown color density gradually increases. The particle size of granular layers presents a declined trend and decreases from

5.74 $\pm$ 0.76 μm for Mg-MOF samples to 2.41 $\pm$ 0.28 μm for Mg/Cu5 samples (Figure 2d). The drop in particle size can be mainly ascribed to the longer length of the Cu–O bond than that of the Mg–O bond, resulting in the distortion and deformation of Mg/Cu-MOF coordination due to the Jahn–Teller effect.[32] In addition, EDS analysis was carried out to detect the surface chemical components, as shown in Figure 2b. Signals of Mg and Cu elements can be inspected, verifying the successful deposition of Mg/Cu-MOF coating on the Zn substrate. The EDS results also indicated the appearance of higher signals of Cu^{2+} in some areas due to an enhanced substitution volume. The detailed chemical components of various coatings are displayed in Figure 2c. Calculation of the atomic content ratio indicated that the Cu^{2+} content increases, and the detailed ratios of Mg/Cu are 6.8, 4.7, and 3.6 in Mg/Cu1, Mg/Cu3, and Mg/Cu5 coatings, respectively.

The XRD and FTIR patterns were recorded to examine the crystallinity structures and functional groups of the surface coatings, as shown in Figure 2e,f. In Figure 2e, the featured peaks of MOF-74 can be observed in all samples with obvious characteristic peaks presenting at 6.8, 11.9, 17.3, 21.9, 24.8, 25.6, and 42°, indicating the successful fabrication of the MOF-74 structure, corresponding to previous studies.[31,33] In addition, the peaks at 6.8 and 11.9° gradually migrate toward lower angles, which could be related to the fact that Cu^{2+} has a greater ionic radius (0.073 nm) than Mg^{2+} (0.072 nm), causing an increase in crystal-plane spacing.[27] Beyond that, the diffraction peaks of ZnO (JCPD No. 36-1451) can also be discovered, the intensities of which are higher for bimetallic coatings than for Mg-MOF coating. The formation of ZnO may be mainly due to the corrosion of the Zn matrix during the hydrothermal procedure.[34] Figure 2f displays the FTIR
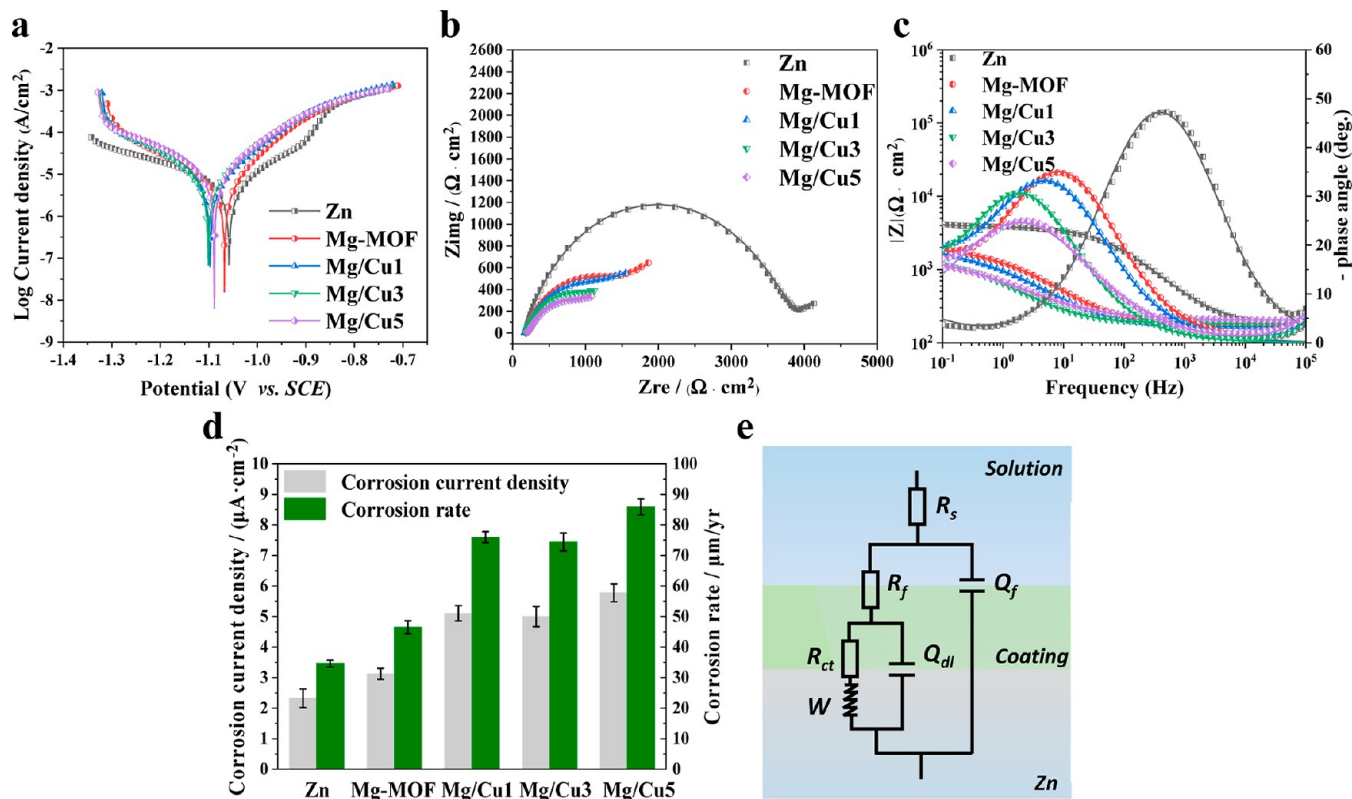
Figure 4. Electrochemical test results of pure Zn and Mg/Cu-MOF-coated samples, (a) PDP curves, (b) Nyquist plots, (c) Bode plots of |Z| or phase angle vs frequency, (d) variation trend of corrosion current density and corrosion rate, and (e) fitted electrical equivalent circuit (EEC) diagram.

patterns of various Mg/Cu-MOF coatings on the pure Zn surface. The presence of a broad peak at ~3446 cm^{-1} can be attributed to the O−H stretching of hydroxyl groups in the organic ligand DHTA, the methanol solvent, and the absorbed water molecules on the sample surface or in the channels of MOF-74.[35] The peak at 1599 cm^{-1} can be mainly ascribed to the stretching vibrations of C═O in the DHTA.[36,37] The shift of the absorption frequency toward a lower wavenumber may be due to the fact that C═O connects the benzene rings to form a conjugated system during the synthesis of MOFs, and the electron cloud density in the system was averaged, leading to the migration of the absorption peak to the direction of a lower wavenumber. Besides, the peaks at 1434, 1224, and 1127 cm^{-1} can be assigned to the stretching vibrations of C═C, C−H, and C−O, respectively.[37−39] The sharp peaks located at 898 and 821 cm^{-1} are derived from the bending vibration peaks of the benzene ring.[40,41] Moreover, the peaks presented at 589 cm^{-1} can be ascribed to the M−O (metal—Mg and Cu) bond.[42]

3.2. Wettability and Adhesion Performance.
To examine the hydrophilicity of different samples, water contact angle measurements were carried out, as displayed in Figure 3a and Figure S2. It can be observed in Figure 3a that the pure Zn surface presents a moderate surface wettability of about 63.6 ± 3.9°. With the deposition of Mg-MOF coating, the sample presents superhydrophilic property (about 7.1 ± 0.2°), which can be attributed to the surface hydroxyl and spongy nanostructures of the MOF-74 structure.[43] With various Mg/Cu-MOF coatings, the water contact angle values decrease with increasing Cu doping. The addition of Cu^{2+} in Mg-MOF partially replaces the position of Mg^{2+}, aggrandizing the pore

volume of the MOF structure.[27] Moreover, the difference in the radius and coordination patterns of Mg^{2+} and Cu^{2+} may also cause microregion flaws and enhance the porosity and specific surface area, resulting in higher surface wettability.[44]

Generally, a strong adhesion force between coatings and the substrate is warranted to avoid coating failure and sustain its multifunctional characteristics. Thus, the binding force of Mg/Cu-MOF coatings on the Zn surface was measured by scratch experiments, as displayed in Figure 3b,c. It can be observed that the coating is damaged from point 1, where wavy accumulation traces form, and the adhesion strength at this place is defined as L_{c1}. As the scratch tests were continued, the coatings began to peel off from the substrate at point 2 locations, at which the binding force is defined as L_{c2}. Generally, the L_{c1} is mainly used to evaluate the cohesion strength of the coating, while the L_{c2} can represent the adhesion strength between the coating and the substrate.[29] With the addition of Cu, the L_{c2} value increases gradually from 5.3 ± 0.1 N for the Mg-MOF samples to 6.0 ± 0.2 N for the Mg/Cu5 samples (Figure 3c). Besides, the peeling areas around the scratch decrease obviously, indicating that the addition of Cu^{2+} helps to improve the adhesion strength between the coating and the substrate. Fang et al. successfully prepared a biomimetic coating of polydopamine (PDA) bonded with poly(lactic-co-glycolic acid) (PLGA) on pure Zn, and the adhesion strength of the coating was about 40.2 mN with good tensile deformation resistance.[45] In comparison, the immobilized Mg/Cu-MOF coatings in this study showed superior adhesion strength. In addition, the oral GBR membrane usually needs to be bent to adapt the shape of the alveolar crest, and maintaining certain integrity under the
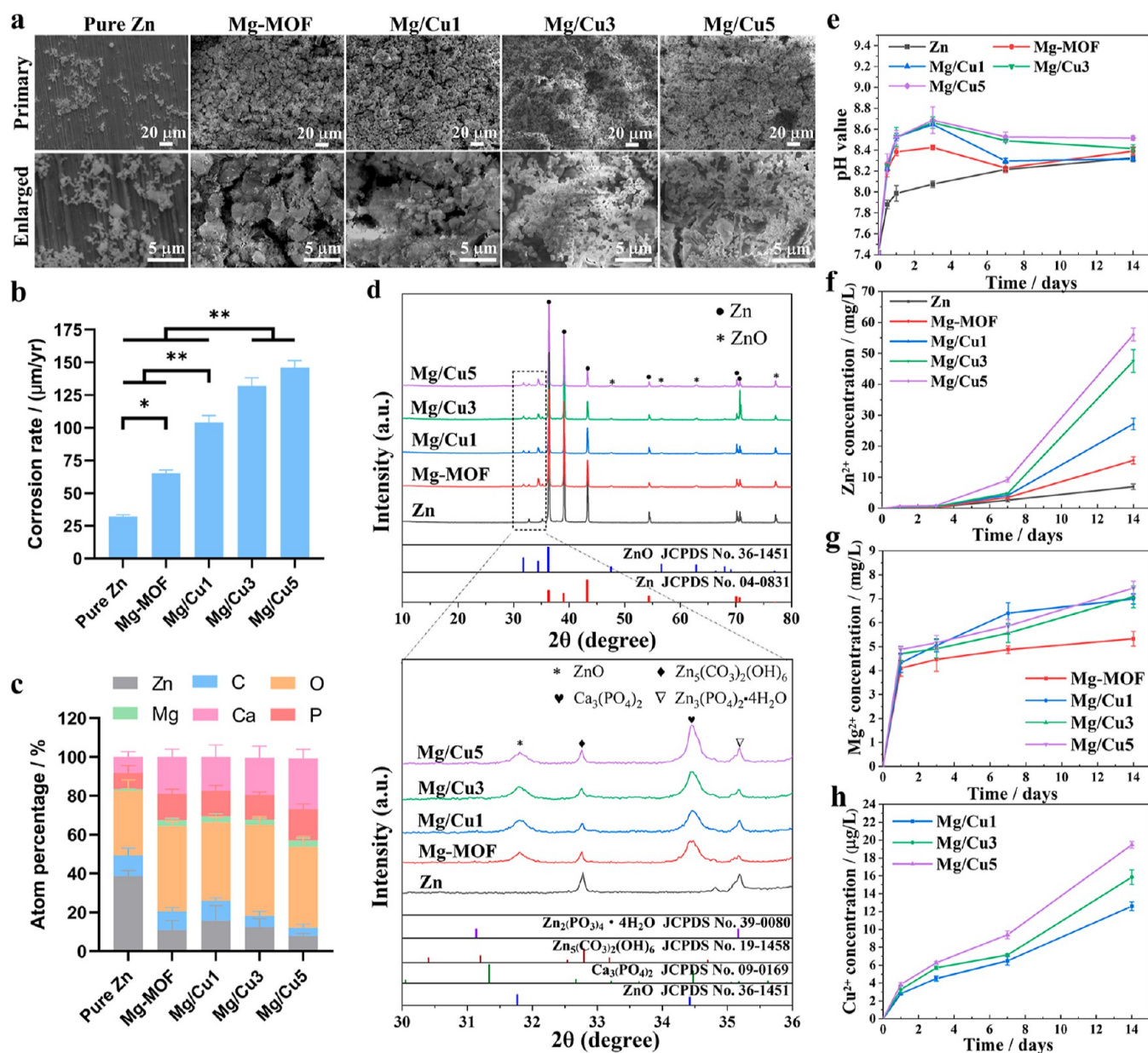
Figure 5. (a) Corrosion surface morphologies of pure Zn and Mg/Cu-MOF-coated samples after immersion in Hank's solution for 14 days (the enlarged pictures are displayed in the bottom line), (b) corrosion rate of the samples, (c) EDS results of surface corrosion products, (d) XRD patterns of pure Zn and coated samples after 14 days of immersion in Hank's solution (the marked region is shown in the bottom line), (e) variation trend of the pH value, and the released (f) Zn^{2+}, (g) Mg^{2+} and (h) Cu^{2+} in the Hank's solution during the whole immersion tests.

action of bending is the key to ensure its better function. Figure 3d shows the morphologies of Mg/Cu-MOF-coated strips after U-bending treatment. Some tiny cracks perpendicular to the direction of bending stress are observed on the granular layer of the Mg-MOF sample. With the increase of added Cu, the number of surface cracks decreases. The coating integrity of the Mg/Cu5 sample can still maintain more than 90% at the microscopic level without peeling-off, which guarantees sound deformation resistance and favorable structural stability during practical application.

3.3. In Vitro Degradation Behavior. To evaluate the degradation behavior of the coated samples, electrochemical approaches, including PDP and EIS tests, were adopted to investigate the impact of Mg/Cu-MOF structures on the degradation of Zn samples, as presented in Figure 4. Accordingly, electrochemical parameters, including the corro-

sion potential (E_{corr}), corrosion current density (i_{corr}), and corrosion rate (CR_{PDP}), were acquired from the PDP curves and are shown in Table S3. The PDP results present close E_{corr} values for all of the tested groups, while the Mg/Cu-MOF-coated samples exhibit a higher corrosion current than the pure Zn in both cathodic and anodic polarization regions (Figure 4a). A higher value of i_{corr} can also be found for the Mg/Cu-MOF-coated samples than that of pure Zn, indicating the accelerated corrosion of the coated samples, as displayed in Figure 4d and Table S3. More detailed information is provided by the Nyquist and Bode plots in Figure 4b,c. The Nyquist plots of the coated samples exhibit a lower impedance, and the impedance radius decreases as the Cu addition increases, indicating a deteriorated corrosion resistance.[8] The Bode plots in Figure 4c confirm that coated samples have a lower module |Z| value at a low frequency than pure Zn. An electrical
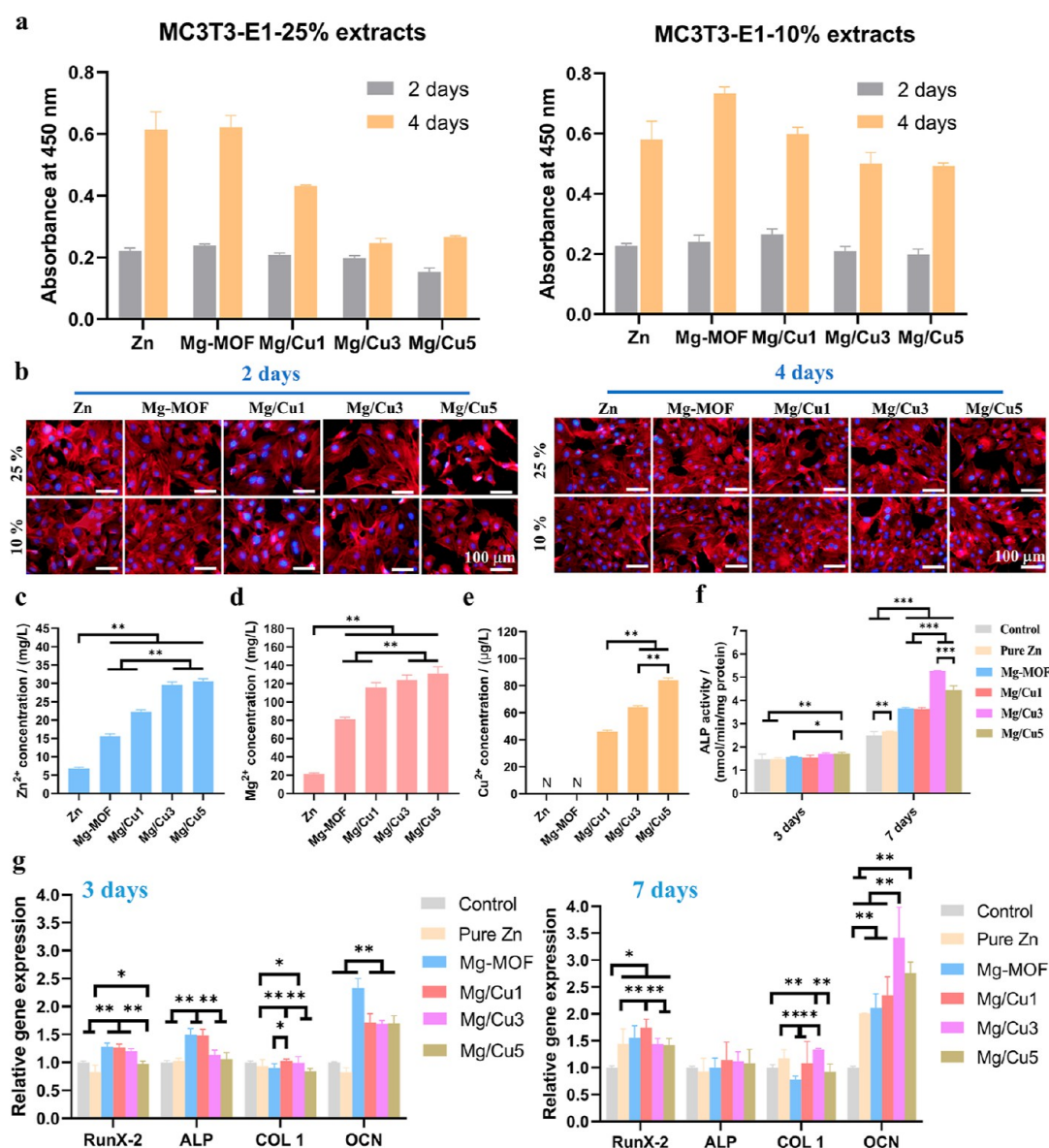
Figure 6. (a) Absorbance (450 nm) of MC3T3-E1 cells cultured with various diluted alloy extracts for 2 and 4 days. (b) Cytoskeletal staining results of MC3T3-E1 cells after 2 or 4 days of culture; representative images of cells stained with rhodamine for actin filaments (red) and DAPI for cell nuclei (blue). Concentrations of (c) Zn^{2+}, (d) Mg^{2+}, and (e) Cu^{2+} in the alloy extracts. (f) ALP activity of pure Zn and Mg/Cu-MOF-coated samples. (g) Relative expression of osteogenic differentiation-related genes, including *COL 1*, *ALP*, *Runx-2*, and *OCN*, in MC3T3-E1 cells cultured in osteogenic medium with diluted alloy extracts (2-fold dilutions) for 3 and 7 days. *$P < 0.05$, **$P < 0.01$, ***$P < 0.001$.

equivalent circuit (EEC, $R_s(Q_f(R_f(Q_{dl}R_{ct}W))))$) was constructed to simulate the impedance results, as displayed in Figure 4e. In this circuit diagram, R_s refers to the solution resistance; Q_f and R_f are related to the capacitance and resistance of the surface coating layer, respectively; Q_{dl} and R_{ct} refer to the double-layer capacitance and resistance associated with the charge-transfer reaction, respectively; and W is the Warburg impedance related to diffusion. The fitted results are presented in Table S4. It can be seen that the R_s values in all groups are close, indicating the validity of the fitted results. The values of Q_f and R_f for the coated samples are significantly lower than those of the pure Zn group, which may suggest the degradation of the MOF coating and the penetration of corrosive medium into the coating/substrate interface.[27] Accordingly, the coated samples possess a lower R_{ct} value (1.1−1.5 kΩ·cm²) than that of pure Zn (2.4 kΩ·cm²). Furthermore, the total resistance value (R_t) of the samples

can be acquired by extrapolating the EIS to the frequency that is sufficiently low ($f \approx 0$).[46] According to the ECC model, R_t can be obtained by the sum of R_f and R_{ct}. With the increase of added Cu amount, the R_t value decreases from 3.7 kΩ·cm² for pure Zn to 1.3 kΩ·cm² for Mg/Cu5 samples, indicating a promoted corrosion impact on Zn substrate with MOF coating.[47]

Figure 5 presents the degradation behaviors of the Mg/Cu-MOF-coated samples during long-term immersion. Enhanced degradation was observed for the MOF-coated samples, demonstrated by the more severe corrosion morphology (Figure 5a), thicker corrosion layer (Figure S3), and higher corrosion rates. Specifically, the corrosion rates of pure Zn, Mg-MOF, Mg/Cu1, Mg/Cu3, and Mg/Cu5 samples are 32.1 ± 1.2, 65.0 ± 2.6, 104.1 ± 5.3, 131.9 ± 6.2, and 146.1 ± 5.2 μm/yr, respectively (Figure 5b). The corrosion rates increase with increasing amount of Cu dopant in coating, which is in

line with the electrochemical corrosion results. The enhanced corrosion (increase of 102.5−355.1%) of the Mg/Cu-MOF-coated samples is attributed to both the porous structure of the MOF coating and its degradation, which cannot block the penetration of physiological fluid effectively. The EDS results also demonstrate significantly higher amounts of Ca and P (Figures 5c and S3). XRD analysis verifies that these surface corrosion products are mainly composed of ZnO, $Ca_3(PO_4)_2$, $Zn_3(PO_4)_2 \cdot 4H_2O$, and $Zn_5(CO_3)_2(OH)_6$ phases (Figure 5d), which is in line with previous reports.[12,28,48] According to previous in vivo studies, it can be discovered that these degradation products show favorable in vivo safety.[11,49,50] Moreover, the diffraction intensity derived from $Ca_3(PO_4)_2$ increases with increasing amount of Cu dopant for Mg/Cu-MOF samples, indicating that the degradation of the MOF coating favors the development and mineralization of the intermediate bioactive apatite layer (Scheme 1). Notably, the degradation of the MOF structure upregulates the pH of the solution. As shown in Figure 5e, the pH of the solution incubated with pure Zn shows a continuous increase during the immersion test, which reached 7.9 at 24 h and gradually increased to 8.3 on day 14. In comparison, the pH value for the Mg/Cu-MOF group increased in the first 3 days, and then decreased to 8.2−8.4 at day 14 with a slight fluctuation. The MOF coating degradation provides an alkaline environment, which promotes the consumption of Zn^{2+} and facilitates the nucleation and precipitation of calcium phosphate and carbonates back to the sample surface.[27,51,52] Hence, calcium phosphate deposition was increased for Mg/Cu-MOF-coated samples. It can be found that the Mg-MOF-coated sample exhibited the burst release of Mg^{2+} within 24 h without any significant increase of Mg^{2+} afterward, indicating that the Mg-MOF coating almost completely degraded at 24 h (Figure 5g). The hybrid Mg/Cu-MOF coating showed a similar Mg^{2+} release profile in 24 h, and the Mg^{2+} release continued with a much slower rate during 1−14 d (Figure 5g). Notably, Zn^{2+}, Mg^{2+}, and Cu^{2+} were released along with the coating degradation (Figure 5f−h). The accumulated amount of Mg^{2+} release for the Mg/Cu-MOF sample reached ∼7 mg/L (0.29 mM), which was ∼39% higher than that for the Mg-MOF sample (Figure 5g). The overall Cu^{2+} release for Mg/Cu-MOF samples was in the range of 12−19 μg/L (0.19−0.30 μM) after 14 days of immersion (Figure 5h). It has been reported that the half-maximal inhibitory concentration (IC$_{50}$) of Cu^{2+} to MC3T3-E1 cells was about 15.9 μM,[53] and the safe Mg^{2+} concentration level for MC3T3-E1 was about 15 mM,[54] indicating good biocompatibility of coated samples.

Degradation could determine the Zn-based membrane performance from the physical properties and biological response. Degradation deteriorates the mechanical integrity and barrier effect of membranes. Guo et al. demonstrated that a pure Zn membrane (30 μm thick) lost less than 30% in thickness and preserved its barrier function after 10 weeks of degradation in a rat calvarial critical-sized bone defect model.[10] Tan et al. reported that a compact corrosion product layer was left after complete degradation of the pure Zn foil, which could act as a secondary phase to the barrier functionality of the membrane and provide a barrier effect for a longer period.[55,56] Moreover, Si et al. fabricated Ca−P-coated Mg-2.0Zn-1.0Gd (wt %) alloys with a degradation rate of 260 μm/yr, and the in vivo results indicated that the alloy can fulfill its task without rupture for 3 months.[57] In this study, the Mg/Cu-MOF-coated samples presented a suitable degradation rate of 65.0−146.1

μm/yr. Assuming the membrane thickness was 30 μm, the degradation period could range from 10 to 22 weeks, which is comparable to the commercial collagen membrane and PLGA membrane.[1] In this context, the Mg/Cu-MOF-coated Zn materials could satisfy the membrane requirement with respect to the barrier effect during bone regeneration. Further evaluation of the biological responses is discussed in the following section.

3.4. Osteogenesis Performance. The cytocompatibility and osteogenesis performance of the Mg/Cu-MOF samples were systematically investigated. Generally, cells at most times did not perform well when directly incubated on the surface of Zn-based materials or incubated in 100% extracts, mainly because the cells are considered to experience a relatively high Zn^{2+} concentration at the Zn−cell interface and induce toxicity. Therefore, 10% and 25% diluted material extracts were used according to the industry consensus, and the MC3T3-E1 proliferation in extracts is shown in Figure 6a. For 25% diluted extracts, MC3T3-E1 cell viability exhibited no significant difference on day 2, then the OD value increased by 2−3 fold in pure Zn, Mg-MOF, and Mg/Cu1 groups on day 4, whereas the cell proliferation in Mg/Cu3 and Mg/Cu5 was significantly reduced. It has been reported that the IC$_{50}$ of Zn^{2+} and Cu^{2+} to MC3T3-E1 cells was about 90.0 and 15.9 μM,[53] respectively, and the safe Mg^{2+} concentration levels for MC3T3-E1 were about 15 mM.[54] Calculated from the ion concentration in extracts, there were about 112.82−116.46 μM of Zn^{2+}, 1.28−1.35 mM of Mg^{2+}, and 0.18−0.33 μM of Cu^{2+} in 25% diluted Mg/Cu3 and Mg/Cu5 extracts (Figure 6c−e). Since Mg^{2+} and Cu^{2+} concentrations in the extracts were far below the IC$_{50}$, the significantly reduced cell proliferation is thus mainly attributed to the enhanced Zn^{2+} release in Mg/Cu3 and Mg/Cu5 groups. After 10% dilution, the number of MC3T3-E1 cells increased continuously during 4 days of culture in all extracts (Figure 6a). Figure 6b shows the fluorescence staining images of MC3T3-E1 cells cultured in different extracts. Full spread of cells is observed in all groups. Despite the smaller number of MC3T3-E1 cells in 25% diluted extracts for Mg/Cu3 and Mg/Cu5 samples, it still presents good cell adhesion with spindle-shaped attachment and pronounced cell-to-cell connections. Recently, Liu et al. reported the bacteriostasis and osteogenesis functions of Mg/Cu-MOF-74 particles, and the results indicated that appropriate Cu doping will enhance the osteogenesis and bacteriostasis properties of particles, while a higher dosage of Cu will inevitably deteriorate the cytocompatibility to SaOS-2 cells,[27] which is in line with results in this study. More importantly, it can be speculated that the flowing body fluid will dilute the released alloy extracts, avoiding the ion accumulation at the implantation sites and further guaranteeing the biosafety of the implants. These results demonstrate the good osteoblast compatibility of hybrid Mg/Cu-MOF-coated samples.

The effects of Mg/Cu-MOF sample extracts on the MC3T3-E1 cells' osteogenic differentiation were further investigated by testing ALP activity (Figure 6f) and the relative expression of osteogenic differentiation-related genes (Figure 6g). According to quantitative analysis, ALP activity in different Mg/Cu-coating groups did not change significantly on day 3, while they were obviously increased on day 7 with the value peaking for the Mg/Cu3 group (Figure 6f). The expression of osteogenic genes, *COL-1*, *ALP*, *Runx-2*, and *OCN* was subsequently evaluated by real-time PCR experiments. It is
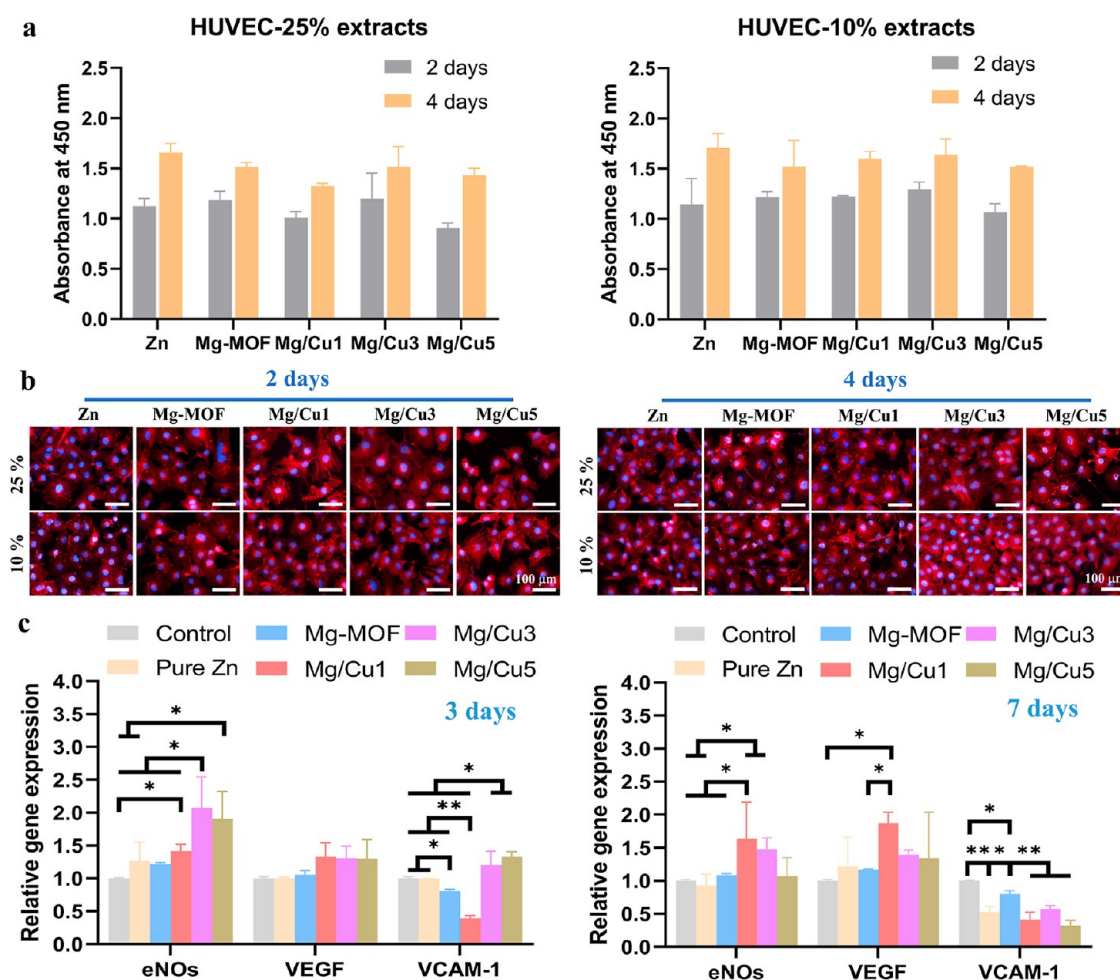
Figure 7. (a) Absorbance (450 nm) of HUVECs cultured with various diluted alloy extracts for 2 or 4 days. (b) Cytoskeletal staining results of HUVECs after 4 days of culture; representative images of cells stained with rhodamine for actin filaments (red) and DAPI for cell. (c) Relative expression of vascularization-related genes, including *eNOs*, *VEGF*, and *VCAM-1* in HUVECs cultured in medium with diluted alloy extracts (2-fold dilutions) for 3 and 7 days. $*P < 0.05$, $**P < 0.01$.

found that gene expression of *Runx-2* and *OCN* is significantly upregulated in different Mg/Cu-coating groups at both time points. This could be explained by the simultaneous release of Mg^{2+} with the degradation of the MOF structure and Zn^{2+} leaching from the Zn substrate. Mg^{2+} could promote osteogenic differentiation by stimulating the formation of neuronal calcitonin gene-related polypeptide-a (CGRP) in both the femoral peripheral cortex and the ipsilateral dorsal root ganglia (DRG).[16] Besides, they exert synergistic effects in osteoinduction by promoting the influx of Mg^{2+} and Zn^{2+} ions into osteoblastic cells and increasing their intracellular amounts.[18,43] It can effectively upregulate integrin $\alpha1$ and integrin $\beta1$ to promote rBMSC adhesion and spreading, stimulate *Runx-2* (an early osteo-differentiation marker), and then enhance *OCN* (a late marker of osteoblast maturation) expression.[58] Of note, higher expression of *Runx-2*, *COL-1*, and *OCN* is correlated with Cu release concentration. On day 7, the expression of *Runx-2* peaks in the Mg/Cu1 group, and *COL-1* and *OCN* peak in the Mg/Cu3 group (Figure 6g). Cu is essential for the metabolism of the skeleton, and Cu deficiency usually causes bone abnormalities. Although different Cu-doped biomaterials have been proven to have a pro-osteogenic effect, as evidenced by the enhanced osteogenic gene expression in vitro, as well as promoted new bone

formation around the implants in vivo, the underlying mechanisms are still unclear.[59,60] One assumption is that Cu^{2+} exhibits progenesis through HIF-1 pathway by mediating the angiogenic and osteogenic phases of bone regeneration.[61] The excessive Cu^{2+} release reduced the cell proliferation and osteogenic differentiation, as shown in the Mg/Cu5 group. Briefly, these results verify that the bimetallic MOF-coated samples remarkably enhanced the osteoconductive capacity of osteoblasts over time, and the increment is concentration-dependent.

3.5. Angiogenesis Ability. Angiogenesis is a critical phase in bone regeneration, providing the function connection between the bone defect and surrounding host tissues.[62] In this perspective, we investigated the ability of Mg/Cu-MOF-coated samples to support angiogenesis. Figure 7a presents the HUVEC proliferation after 2 and 4 days of culture in 10% and 25% diluted sample extracts. It can be found that HUVECs showed comparable proliferation rate in all groups at each time point. Cytoskeletal staining further revealed the fully spread cell morphology with pronounced cell-to-cell connections in all groups (Figure 7b). Shearier et al. discovered relatively higher Zn^{2+} tolerance for human endothelial cells (HAEC) which indicate 50% survival at Zn^{2+} concentrations of $\sim265\ \mu M$.[63] In this study, the Zn^{2+} concentrations in different extracts (25%
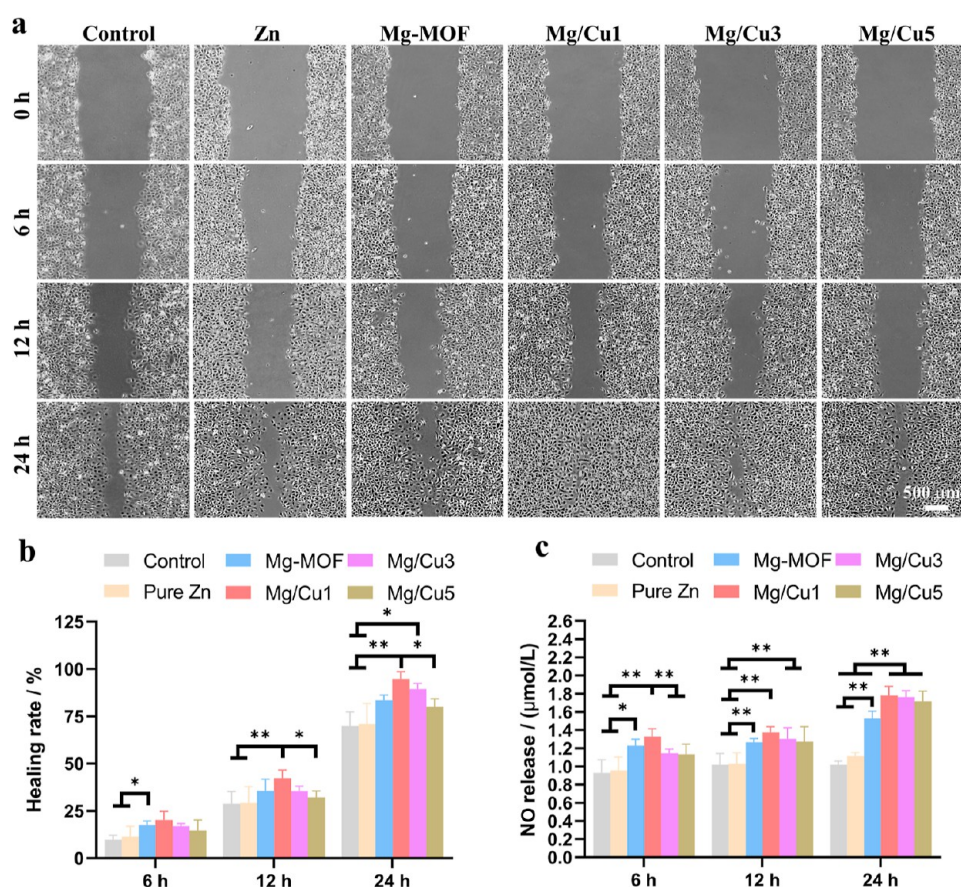
Figure 8. (a) Optical pictures showing the effect of different alloy extracts on the cell migration rate of HUVECs, (b) corresponding healing rate values, and (c) NO release of HUVECs determined by a typical Griess reagent assay. *$P < 0.05$, **$P < 0.01$.

diluted) ranged 26.0−116.5 μM, which is favorable for cell survival and proliferation and thus accounting for the sound cytocompatibility to HUVECs in all groups (Figure 7a). Then, the expression of angiogenic-related markers was also analyzed. The Mg/Cu group significantly increased the expression of angiogenetic genes *eNOs* and *VEGF* with respect to the Cu free groups at all time points (Figure 7c). The downregulated expression of *VCAM-1* was also observed for all the materials groups with respect to the control, indicating the reduced inflammatory response. *eNOs* and *VEGF* expressions peaked for the Mg/Cu1 group on day 7.

An evaluation was next made in terms of cell migration and NO release to further evaluate the angiogenic capacity. The cell images and quantitative cell numbers in wounding regions are illustrated in Figure 8a,b. HUVECs exhibited better migration ability in all the Mg/Cu coating groups as compared to the pure Zn and control group. NO has been reported to have a significant effect toward promoting the adhesion, proliferation, and migration of endothelial cells. Significantly promoted NO production of HUVECs was observed for the Cu-containing coating groups (Figure 8c), suggesting their better migration capacity. Among different Cu-containing groups, the Mg/Cu1 group displays the fastest migratory response, and the scratch almost healed at 24 h.

Combined with the ion concentrations in Mg/Cu groups (Figure 6c−e), Cu^{2+} could play a central role in enhancing the angiogenic activity, while Mg^{2+} and Zn^{2+} exhibited not significant positive effects on angiogenesis. Cu^{2+}, one of the bioactive ions, has been shown to promote angiogenesis by

mimicking a hypoxia microenvironment, and it can have an effect at extremely low concentrations.[64,65] It helps to increase the proliferation and differentiation of osteoblastic cells in implant applications, and a lack of Cu^{2+} can cause bone loss.[66,67] Besides that, Cu^{2+} also has the potential to inhibit collagen fibril formation while promoting angiogenesis, which would accelerate the infiltration of blood vessels into the bone defect and is conducive to subsequent bone regeneration.[21,22] Beyond that, Cu^{2+} is involved in the main stages of angiogenesis by activating signaling pathways related to endothelial cell proliferation, differentiation, and migration.[22] In fact, Cu-loaded membranes present a higher capacity to stimulate angiogenesis and bone regeneration compared to Cu-free ones.[22,68] Considering the dosage-dependent toxicity of Cu^{2+}, the amount and kinetics of Cu release are crucial for compatibility with the tissues. Mg/Cu-MOF coatings exhibited a very slow Cu release (0.85−1.35 μg/d) that fell into the favorable Cu concentration range for EC proliferation (Figure 5h).[69] Accordingly, our findings demonstrated enhanced eNOs secretion and NO generation in the Cu-containing groups compared to the Cu-free groups. The angiogenesis-related gene expression and migration ability peaked in the Mg/Cu1 group. Therefore, according to the cytocompatibility results (Figures 6 and 7), it can be confirmed that an appropriate Cu dopant is beneficial to both osteogenesis and angiogenesis performances of implants, corresponding to a recent study reported by Xiang et al.[70] Higher corrosion rates and coordinated release of multiple metal ions may account for the best cytocompatibility performance of Mg/Cu1 samples.
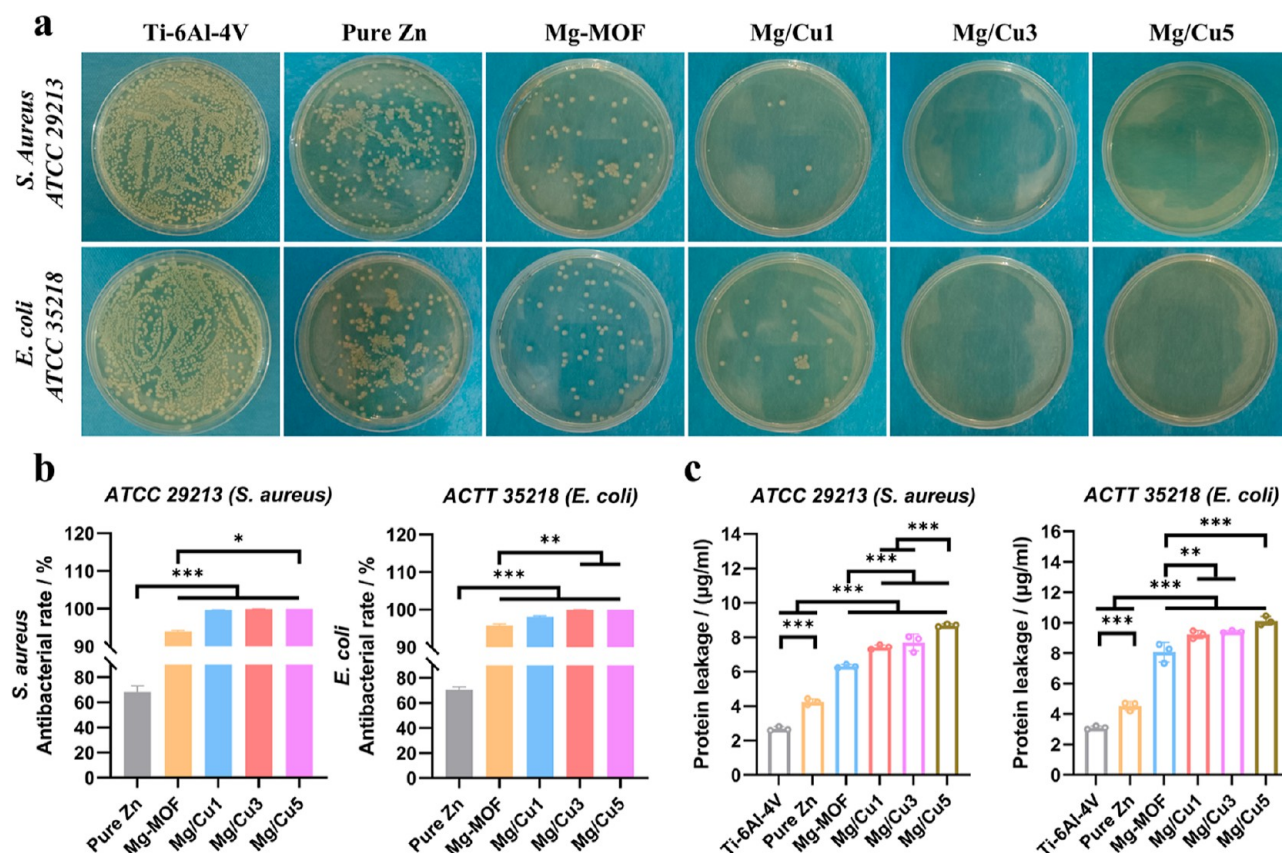
Figure 9. (a) Representative images of bacterial growth on the surface of samples after 24 h of culture, (b) antibacterial rate of different samples derived by the plate counting method, and (c) protein leakage of *S. aureus* and *E. coli* measured by the BCA protein assay kit. *$P < 0.05$, **$P < 0.01$, ***$P < 0.001$.

3.6. In Vitro and In Vivo Bacteriostatic Activity. It has been verified that bacterial invasion is mostly responsible for the negative consequences of barrier membrane exposure on neighboring tissues. Inflammatory response caused by bacterial infection can inhibit osteoblast growth, hence impairing the bone regenerative outcomes and even resulting in surgical failure. It is possible to ensure or improve bone healing by preventing bacterial invasion.

The bacteriostatic activity of Mg/Cu-MOF-coated samples against *S. aureus* and *E. coli* was examined by the plating dilution method. There were fewer *S. aureus* and *E. coli* colonies for various hybrid Mg/Cu-MOF samples than for pure Zn and Mg-MOF ones. With a higher Cu dopant amount, the colony numbers further decreased (Figure 9a). Further bacteriostatic rate analysis indicated similar tendencies, as shown in Figure 9b. The percent reduction of *S. aureus* and *E. coli* for the Mg/Cu1 group was 99.7% and 98.1% after 24 h of culture. The destruction of bacterial membrane was usually accompanied by the leakage of cytoplasm, such as intracellular proteins.[71] Hence, the content of protein leakage was measured to evaluate the bacterial membrane permeability in different groups. In Figure 9c, the results indicated that increased Cu addition significantly destroyed the bacterial membrane structure and aggrandized permeability.

To further verify the in vivo bacteriostatic ability of MOF-coated samples, a hypodermic bacterial infection model and *S. aureus* strains were employed, as displayed in Figure 10a. The plate counting results indicated that pure Zn presented moderate antibacterial ability against *S. aureus* in vivo (Figure

10b). In comparison, Mg/Cu1 samples presented a strong bacteriostatic property with few viable strains existing in the agar plate. In addition, it could be calculated that the antibacterial rates of pure Zn and Mg/Cu1 samples were around 59.3 ± 1.4 and 98.7 ± 0.6%, respectively, indicating an outstanding in vivo bacteriostatic activity of Mg/Cu1 samples under the synergistic action of Zn^{2+} and Cu^{2+}.

Beyond that, to observe the inflammation responses and wound healing outcomes, the peri-implant subcutaneous tissue was stained by H&E, Masson's trichrome, and immunohistochemistry staining (IL-1β and CD31), as illustrated in Figures 10d and S4. In the control group, typical features of tissue infection with extensive lymphocyte and neutrophil infiltrations could be observed. In comparison, reduced inflammation response was found in the pure Zn group. For the Mg/Cu1 group, it indicated a weaker inflammatory response with less inflammatory cell infiltration in the H&E staining. The IL-1β immunohistochemistry staining results indicated that Mg/Cu1 samples presented an anti-inflammatory effect. Furthermore, Masson's trichrome staining was used to observe the peri-implant collagen deposition. Among all groups, the subcutaneous tissue around the Mg/Cu1 group presented numerous and closely interwoven collagen fibers, indicating that the samples induced a better collagen deposition, which is beneficial to wound healing and inhibition of bacterial infection. After 10 days of surgeries, the number of blood vessels in the coated groups increased, and the diameter of the blood vessels also became larger (Figure S4, denoted by blue arrows), indicating more mature vascularization. The Mg/
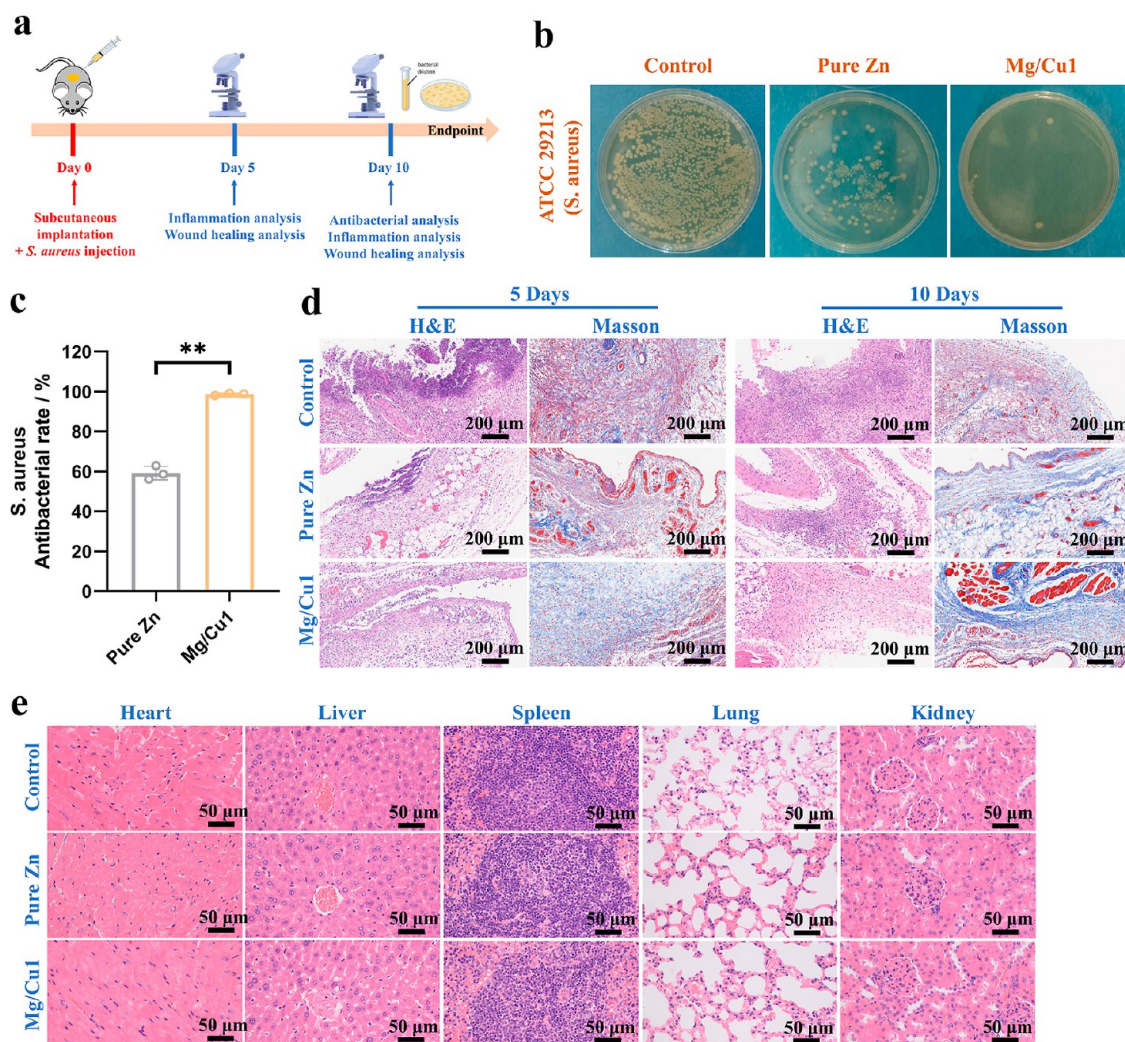
Figure 10. (a) Diagram illustrating the detailed process of in vivo subcutaneous implantation experiments, (b) representative images of bacteria grown on the sample surface after surgery, (c) in vivo antibacterial rate of pure Zn and Mg/Cu1 samples, (d) histological section results (H&E and Masson's trichrome) of surrounding tissues after 5 and 10 days of in vivo implantation, and (e) H&E staining results of rat heart, kidneys, liver, lungs, and spleen after surgery. $**P < 0.01$.

Cu1-coated samples appeared to have a promoted pro-angiogenesis effect. Additionally, no abnormality was observed in the pathological sections in all groups (Figure 10e), verifying the satisfactory in vivo biosafety of Mg/Cu1 samples.

The high antibacterial ability of Mg/Cu-MOF-coated samples can be explained by the following reasons. First, Mg/Cu MOFs coating accelerated the degradation of the Zn substrate and resulted in a higher amount of Zn^{2+} release (Figure 5f). Cu^{2+} was also released as the MOF structure deteriorated (Figure 5h). The released Zn^{2+} or Cu^{2+} could be electrostatically adsorbed on the negatively charged cell wall, destroying the basic structure of the peptidoglycan layer.[14,72] Besides, the ions could react with the sulfhydryl groups on the membrane protein to inactivate the protein, destroying the bacterial membrane and leading to the leakage of intracellular proteins (Figure 9c).[72] As a result, the ions could enter the cell, inhibiting the synthesis of proteins and enzymes related to cell function and hampering the proliferation of bacterial cells. Furthermore, the ions might cause the formation of intracellular reactive oxygen species (ROS), thereby causing lipid peroxidation, inactivating membrane proteins/enzymes, and resulting in DNA damage.[73] More importantly, the ions might cause impairment of the respiratory chain activity and the gene replication process of bacteria.[22,74] Second, the degradation of external Mg/Cu-MOF coating would induce a local alkaline microenvironment around the implant as well. Protons would become depleted in this alkaline microenvironment, preventing them from accessing the bacterial membrane via the proton pumps along the electrochemical gradient. As a result, the F-type H^+-ATPase on the bacterial membrane would cease generating ATP, resulting in energy loss and even bacterial death.[75] Based on the above results, the immobilization of Mg/Cu-MOF coatings could boost the antibiotic ability of Zn substrate due to the combined effect of long-lasting Zn^{2+} and Cu^{2+} leaching, as well as an induced alkaline microenvironment (Scheme 1). Moreover, the prevention of implant-related infection can also avoid excessive inflammatory responses and resultant macrophage migration, which deteriorate endothelial dysfunction, vascularization, and related osteogenesis.

Taken all together, Mg/Cu-MOF coating exhibits component controllability, good binding force, and structural stability, ensuring the membrane's spatial stability and bioadaptability during application. The in vitro tests demonstrated that the hybrid Mg/Cu-MOF-modified Zn samples (especially Mg/

Cu1) exhibited superior multifunction of osteogenesis, angiogenesis, and bacteriostasis properties due to the enriched degradation products (Zn^{2+}, Mg^{2+}, and Cu^{2+}) and alkaline microenvironment. The antibacterial activity and inflammatory response of Mg/Cu1 were further demonstrated in vivo. As such, further in vivo studies will be carried out to comprehensively investigate the in vivo degradation behavior, angiogenesis, and bone regeneration activity of the Mg/Cu-MOF-coated Zn membrane. Moreover, more attention should be focused on the interaction between cells/bacteria and MOF particles in the future.

4. CONCLUSIONS

In this study, various bimetallic Mg/Cu-MOF coatings were successfully fabricated on pure Zn, aiming to promote osteogenesis, angiogenesis, and antibacterial activity of the Zn substrate. The results indicated that the degradation rate and water stability of Mg/Cu-MOF coating could be regulated by controlling the feeding ratio of Cu^{2+}. Mg/Cu-MOF coating significantly promoted osteoblast differentiation, enhanced the vascularization of endothelial cells, and presented superior antibacterial activity. It was mainly due to the synergistic action of Zn^{2+}, Mg^{2+}, Cu^{2+}, and the local alkaline microenvironment. Among them, Mg/Cu1 showed the best comprehensive performance. In vivo, Mg/Cu1 presented an outstanding antibacterial function and thus regulated the inflammatory responses. Overall, the bimetallic Mg/Cu-MOF coating provided a robust and facile pathway for designing biofunctional coatings on Zn, which is beneficial to the development of a novel Zn-based absorbable GBR membrane.

■ ASSOCIATED CONTENT

ⓈI Supporting Information

The Supporting Information is available free of charge at https://pubs.acs.org/doi/10.1021/acsami.3c16970.

> Schematic diagram illustrating the U-bending deformation process of Mg/Cu-MOF-coated pure Zn foils; morphologies of water contact angles of pure Zn and Mg/Cu-MOF-coated samples; SEM pictures illustrating the cross section of the coating in different groups; immunohistochemistry staining images of control, pure Zn, and Mg/Cu1 groups after surgery for 5 days (IL-1β) and 10 days (CD31); chemical components of reaction solution in different alloy groups; primer sequences of target mRNA and GADPH; polarization data of Zn and Mg/Cu-MOF-coated samples in Hank's solution; and electrochemical fitting results of Zn and Mg/Cu-MOF-coated samples in Hank's solution (PDF)

■ AUTHOR INFORMATION

Corresponding Authors

Xuenan Gu − *Key Laboratory of Biomechanics and Mechanobiology (Beihang University), Ministry of Education, Beijing Advanced Innovation Center for Biomedical Engineering, School of Biological Science and Medical Engineering, Beihang University, Beijing 100083, China;* ⓞ orcid.org/0000-0003-4516-9777; Email: xngu@buaa.edu.cn

Yufeng Zheng − *School of Materials Science and Engineering, Peking University, Beijing 100871, China;* ⓞ orcid.org/0000-0002-7402-9979; Email: yfzheng@pku.edu.cn

Authors

Kai Chen − *Key Laboratory of Biomechanics and Mechanobiology (Beihang University), Ministry of Education, Beijing Advanced Innovation Center for Biomedical Engineering, School of Biological Science and Medical Engineering, Beihang University, Beijing 100083, China; School of Materials Science and Engineering, Peking University, Beijing 100871, China*

Yifan Wang − *Key Laboratory of Biomechanics and Mechanobiology (Beihang University), Ministry of Education, Beijing Advanced Innovation Center for Biomedical Engineering, School of Biological Science and Medical Engineering, Beihang University, Beijing 100083, China*

Hongyan Tang − *Key Laboratory of Biomechanics and Mechanobiology (Beihang University), Ministry of Education, Beijing Advanced Innovation Center for Biomedical Engineering, School of Biological Science and Medical Engineering, Beihang University, Beijing 100083, China*

Xufeng Niu − *Key Laboratory of Biomechanics and Mechanobiology (Beihang University), Ministry of Education, Beijing Advanced Innovation Center for Biomedical Engineering, School of Biological Science and Medical Engineering, Beihang University, Beijing 100083, China;* ⓞ orcid.org/0000-0003-2669-2028

Hongtao Yang − *School of Engineering Medicine, Beihang University, Beijing 100083, China*

Yanjie Bai − *Stomatology Department, Peking University Third Hospital, Beijing 100191, China*

Complete contact information is available at:
https://pubs.acs.org/10.1021/acsami.3c16970

Author Contributions

Kai Chen: Writing—original draft, investigation, and data curation. **Yifan Wang:** Methodology, investigation, and data curation. **Hongyan Tang:** Investigation and formal analysis. **Xufeng Niu:** Investigation and formal analysis. **Hongtao Yang:** Investigation and formal analysis. **Yanjie Bai:** Investigation and formal analysis. **Xuenan Gu:** conceptualization, methodology, resources, supervision, project administration, and funding acquisition. **Yufeng Zheng:** Supervision and project administration.

Notes

The authors declare no competing financial interest.

■ ACKNOWLEDGMENTS

■ REFERENCES

(1) Aprile, P.; Letourneur, D.; Simon-Yarza, T. Membranes for Guided Bone Regeneration: A Road from Bench to Bedside. *Adv. Healthcare Mater.* **2020**, *9* (19), 2000707.

(2) Xia, D.; Yang, F.; Zheng, Y.; Liu, Y.; Zhou, Y. Research status of biodegradable metals designed for oral and maxillofacial applications: A review. *Bioact. Mater.* **2021**, *6* (11), 4186−4208.

(3) Bottino, M. C.; Thomas, V.; Schmidt, G.; Vohra, Y. K.; Chu, T.-M. G.; Kowolik, M. J.; Janowski, G. M. Recent advances in the development of GTR/GBR membranes for periodontal regeneration—A materials perspective. *Dent. Mater.* **2012**, *28* (7), 703−721.

(4) Chen, K.; Zhao, Y.; Liu, C.; Li, Q.; Bai, Y.; Li, P.; Wang, C.; Gu, X.; Fan, Y. Novel Mg-Ca-La alloys for guided bone regeneration:

Mechanical performance, stress corrosion behavior and biocompatibility. *Mater. Today Commun.* **2022**, *32*, 103949.

(5) Chen, K.; Zhao, L.; Sun, J.; Gu, X.; Huang, C.; Su, H.; Fan, Y. Utilizing biodegradable alloys as guided bone regeneration (GBR) membrane: Feasibility and challenges. *Sci. China Mater.* **2022**, *65* (10), 2627−2646.

(6) Chen, K.; Zhao, L.; Huang, C.; Yin, X.; Zhang, X.; Li, P.; Gu, X.; Fan, Y. Recent Advances in the Development of Magnesium-Based Alloy Guided Bone Regeneration (GBR) Membrane. *Metals* **2022**, *12*, 2074.

(7) Li, Z.; Ruan, C.; Niu, X. Collagen-based bioinks for regenerative medicine: Fabrication, application and prospective. *Med. Nov. Technol. Devices* **2023**, *17*, 100211.

(8) Chen, K.; Zhou, G.; Li, Q.; Tang, H.; Wang, S.; Li, P.; Gu, X.; Fan, Y. In vitro degradation, biocompatibility and antibacterial properties of pure zinc: assessing the potential of Zn as a guided bone regeneration membrane. *J. Mater. Chem. B* **2021**, *9* (25), 5114−5127.

(9) Tong, X.; Han, Y.; Zhu, L.; Zhou, R.; Lin, Z.; Wang, H.; Huang, S.; Li, Y.; Ma, J.; Wen, C.; Lin, J. ZnP-Coated Zn−1Cu−0.1Ti Membrane with High Strength-Ductility, Antibacterial Ability, Cytocompatibility, and Osteogenesis for Biodegradable Guided Bone Regeneration Applications. *Adv. Funct. Mater.* **2023**, *33* (31), 2214657.

(10) Guo, H.; Xia, D.; Zheng, Y.; Zhu, Y.; Liu, Y.; Zhou, Y. A pure zinc membrane with degradability and osteogenesis promotion for guided bone regeneration: In vitro and in vivo studies. *Acta Biomater.* **2020**, *106*, 396−409.

(11) Yang, H.; Jia, B.; Zhang, Z.; Qu, X.; Li, G.; Lin, W.; Zhu, D.; Dai, K.; Zheng, Y. Alloying design of biodegradable zinc as promising bone implants for load-bearing applications. *Nat. Commun.* **2020**, *11* (1), 401.

(12) Chen, K.; Ge, W.; Zhao, L.; Kong, L.; Yang, H.; Zhang, X.; Gu, X.; Zhu, C.; Fan, Y. Endowing biodegradable Zinc implants with dual-function of antibacterial ability and osteogenic activity by micro-addition of Mg and Ag (≤ 0.1 wt.%). *Acta Biomater.* **2023**, *157*, 683−700.

(13) Zhu, D.; Su, Y.; Young, M. L.; Ma, J.; Zheng, Y.; Tang, L. Biological Responses and Mechanisms of Human Bone Marrow Mesenchymal Stem Cells to Zn and Mg Biomaterials. *ACS Appl. Mater. Interfaces* **2017**, *9* (33), 27453−27461.

(14) Ning, C.; Wang, X.; Li, L.; Zhu, Y.; Li, M.; Yu, P.; Zhou, L.; Zhou, Z.; Chen, J.; Tan, G.; Zhang, Y.; Wang, Y.; Mao, C. Concentration Ranges of Antibacterial Cations for Showing the Highest Antibacterial Efficacy but the Least Cytotoxicity against Mammalian Cells: Implications for a New Antibacterial Mechanism. *Chem. Res. Toxicol.* **2015**, *28* (9), 1815−1822.

(15) Qu, X.; Yang, H.; Jia, B.; Yu, Z.; Zheng, Y.; Dai, K. Biodegradable Zn-Cu alloys show antibacterial activity against MRSA bone infection by inhibiting pathogen adhesion and biofilm formation. *Acta Biomater.* **2020**, *117*, 400−417.

(16) Zhang, Y.; Xu, J.; Ruan, Y. C.; Yu, M. K.; O'Laughlin, M.; Wise, H.; Chen, D.; Tian, L.; Shi, D.; Wang, J.; Chen, S.; Feng, J. Q.; Chow, D. H. K.; Xie, X.; Zheng, L.; Huang, L.; Huang, S.; Leung, K.; Lu, N.; Zhao, L.; Li, H.; Zhao, D.; Guo, X.; Chan, K.; Witte, F.; Chan, H. C.; Zheng, Y.; Qin, L. Implant-derived magnesium induces local neuronal production of CGRP to improve bone-fracture healing in rats. *Nat. Med.* **2016**, *22* (10), 1160−1169.

(17) Tang, H.; Li, Q.; Li, M.; Gu, X.; Cheng, C.; Fan, Y. In vitro and in vivo evaluation of micro-alloyed magnesium for potential application in alveolar bone fixation screws. *J. Mater. Sci. Technol.* **2023**, *144*, 62−69.

(18) Yu, Y.; Jin, G.; Xue, Y.; Wang, D.; Liu, X.; Sun, J. Multifunctions of dual Zn/Mg ion co-implanted titanium on osteogenesis, angiogenesis and bacteria inhibition for dental implants. *Acta Biomater.* **2017**, *49*, 590−603.

(19) Xu, X.; Sun, X.; Tan, X.; Xue, R.; Zhang, L.; Liu, L. Osteo-angiogenic and antibacterial activity of a multifunctional micro-porous coating on zirconium alloy. *Appl. Surf. Sci.* **2022**, *604*, 154465.

(20) Guo, G.; Xu, Q.; Zhu, C.; Yu, J.; Wang, Q.; Tang, J.; Huan, Z.; Shen, H.; Chang, J.; Zhang, X. Dual-temporal bidirectional immunomodulation of Cu-Zn Bi-layer nanofibrous membranes for sequentially enhancing antibacterial activity and osteogenesis. *Appl. Mater. Today* **2021**, *22*, 100888.

(21) Saghiri, M. A.; Asatourian, A.; Orangi, J.; Sorenson, C. M.; Sheibani, N. Functional role of inorganic trace elements in angiogenesis—Part II: Cr, Si, Zn, Cu, and S. *Crit. Rev. Oncol. Hematol.* **2015**, *96* (1), 143−155.

(22) Cordeiro, J. M.; Barão, V. A.; de Avila, E. D.; Husch, J. F. A.; Yang, F.; van den Beucken, J. J. J. P. Tailoring Cu2+-loaded electrospun membranes with antibacterial ability for guided bone regeneration. *Biomater. Adv.* **2022**, *139*, 212976.

(23) Neufeld, B. H.; Neufeld, M. J.; Lutzke, A.; Schweickart, S. M.; Reynolds, M. M. Metal-Organic Framework Material Inhibits Biofilm Formation of Pseudomonas aeruginosa. *Adv. Funct. Mater.* **2017**, *27* (34), 1702255.

(24) Chen, M.; Wang, D.; Li, M.; He, Y.; He, T.; Chen, M.; Hu, Y.; Luo, Z.; Cai, K. Nanocatalytic Biofunctional MOF Coating on Titanium Implants Promotes Osteoporotic Bone Regeneration through Cooperative Pro-osteoblastogenesis MSC Reprogramming. *ACS Nano* **2022**, *16* (9), 15397−15412.

(25) Zhu, Z.; Jiang, S.; Liu, Y.; Gao, X.; Hu, S.; Zhang, X.; Huang, C.; Wan, Q.; Wang, J.; Pei, X. Micro or nano: Evaluation of biosafety and biopotency of magnesium metal organic framework-74 with different particle sizes. *Nano Res.* **2020**, *13* (2), 511−526.

(26) Robinson, D. A.; Griffith, R. W.; Shechtman, D.; Evans, R. B.; Conzemius, M. G. In vitro antibacterial properties of magnesium metal against Escherichia coli, Pseudomonas aeruginosa and Staphylococcus aureus. *Acta Biomater.* **2010**, *6* (5), 1869−1877.

(27) Liu, J.; Tan, Y.; Shen, E.; Liu, B.; Tian, Y.; Liang, L.; Yan, X.; Wu, H. Highly water-stable bimetallic organic framework MgCu-MOF74 for inhibiting bacterial infection and promoting bone regeneration. *Biomed. Mater.* **2022**, *17* (6), 065026.

(28) Chen, K.; Gu, X.; Sun, H.; Tang, H.; Yang, H.; Gong, X.; Fan, Y. Fluid-induced corrosion behavior of degradable zinc for stent application. *Journal of Materials Science & Technology* **2021**, *91*, 134−147.

(29) Zhang, S.; Xianting, Z.; Yongsheng, W.; Kui, C.; Wenjian, W. Adhesion strength of sol-gel derived fluoridated hydroxyapatite coatings. *Surf. Coat. Technol.* **2006**, *200* (22−23), 6350−6354.

(30) Huang, C.; Li, D.; Song, J.; Chen, K.; Wang, X.; Zhao, F.; Gu, X.; Xie, X.; Fan, Y. Dual-functional coatings on magnesium alloys: Enhancing corrosion behavior under stress and osteogenic effect in osteoporotic rats. *Appl. Mater. Today* **2023**, *30*, 101723.

(31) Campbell, J.; Tokay, B. Controlling the size and shape of Mg-MOF-74 crystals to optimise film synthesis on alumina substrates. *Microporous Mesoporous Mater.* **2017**, *251*, 190−199.

(32) Ling, J.; Zhou, A.; Wang, W.; Jia, X.; Ma, M.; Li, Y. One-Pot Method Synthesis of Bimetallic MgCu-MOF-74 and Its CO_2 Adsorption under Visible Light. *ACS Omega* **2022**, *7* (23), 19920−19929.

(33) Sanz, R.; Martínez, F.; Orcajo, G.; Wojtas, L.; Briones, D. Synthesis of a honeycomb-like Cu-based metal-organic framework and its carbon dioxide adsorption behaviour. *Dalton Trans.* **2013**, *42* (7), 2392−2398.

(34) Mao, M.; Zhu, S.; Zhang, L.; Liu, F.; Kong, L.; Xue, Y.; Rotello, V. M.; Han, Y. An Extracellular Matrix-like Surface for Zn Alloy to Enhance Bone Regeneration. *ACS Appl. Mater. Interfaces* **2022**, *14* (38), 43955−43964.

(35) Cheng, X.; Zhao, P.; Zhang, M.; Wang, S.; Liu, M.; Liu, F. Fabrication of robust and bifunctional cyclotriphosphazene-based periodic mesoporous organosilicas for efficient CO_2 adsorption and catalytic conversion. *Chem. Eng. J.* **2021**, *418*, 129360.

(36) Gao, Z.; Liang, L.; Zhang, X.; Xu, P.; Sun, J. Facile One-Pot Synthesis of Zn/Mg-MOF-74 with Unsaturated Coordination Metal Centers for Efficient CO_2 Adsorption and Conversion to Cyclic Carbonates. *ACS Appl. Mater. Interfaces* **2021**, *13* (51), 61334−61345.

(37) Wang, Z.; Xu, J.; Yang, J.; Xue, Y.; Dai, L. Ultraviolet/ozone treatment for boosting OER activity of MOF nanoneedle arrays. *Chem. Eng. J.* **2022**, *427*, 131498.

(38) Tran, Y. B. N.; Nguyen, P. T. K.; Luong, Q. T.; Nguyen, K. D. Series of M-MOF-184 (M = Mg, Co, Ni, Zn, Cu, Fe) Metal-Organic Frameworks for Catalysis Cycloaddition of CO2. *Inorg. Chem.* **2020**, *59* (22), 16747−16759.

(39) Firoozi, M.; Rafiee, Z.; Dashtian, K. New MOF/COF Hybrid as a Robust Adsorbent for Simultaneous Removal of Auramine O and Rhodamine B Dyes. *ACS Omega* **2020**, *5* (16), 9420−9428.

(40) Liu, Y.; Zhang, J.; Liu, Z.; Li, Z.; Yue, Z. Thermally activated polymerization behavior of bisphenol-S/methylamine-based benzox-azine. *J. Appl. Polym. Sci.* **2012**, *124* (1), 813−822.

(41) Yin, X.; Huang, A.; Zhang, S.; Liu, R.; Ma, F. Identification of Three Dalbergia Species Based on Differences in Extractive Components. *Molecules* **2018**, *23* (9), 2163.

(42) Gao, Z.; Zhang, X.; Xu, P.; Sun, J. Dual hydrogen-bond donor group-containing Zn-MOF for the highly effective coupling of CO2 and epoxides under mild and solvent-free conditions. *Inorg. Chem. Front.* **2020**, *7* (10), 1995−2005.

(43) Shen, X.; Zhang, Y.; Ma, P.; Sutrisno, L.; Luo, Z.; Hu, Y.; Yu, Y.; Tao, B.; Li, C.; Cai, K. Fabrication of magnesium/zinc-metal organic framework on titanium implants to inhibit bacterial infection and promote bone regeneration. *Biomaterials* **2019**, *212*, 1−16.

(44) Barin, G.; Krungleviciute, V.; Gutov, O.; Hupp, J. T.; Yildirim, T.; Farha, O. K. Defect Creation by Linker Fragmentation in Metal-Organic Frameworks and Its Effects on Gas Uptake Properties. *Inorg. Chem.* **2014**, *53* (13), 6914−6919.

(45) Fang, H.; Qi, X.; Zhou, S.; Yang, S.; Hang, C.; Tian, Y.; Wang, C. High-Efficient Vacuum Ultraviolet-Ozone Assist-Deposited Poly-dopamine for Poly(lactic-co-glycolic acid)-Coated Pure Zn toward Biodegradable Cardiovascular Stent Applications. *ACS Appl. Mater. Interfaces* **2022**, *14* (2), 3536−3550.

(46) Liu, L.; Meng, Y.; Dong, C.; Yan, Y.; Volinsky, A. A.; Wang, L. N. Initial formation of corrosion products on pure zinc in simulated body fluid. *J. Mater. Sci. Technol.* **2018**, *34*, 2271−2282.

(47) Mo, X.; Qian, J.; Chen, Y.; Zhang, W.; Xian, P.; Tang, S.; Zhou, C.; Huang, N.; Ji, H.; Luo, E.; Zhang, H.; Wan, G. Corrosion and degradation decelerating alendronate embedded zinc phosphate hybrid coating on biodegradable Zn biomaterials. *Corros. Sci.* **2021**, *184*, 109398.

(48) Bakhsheshi-Rad, H. R.; Hamzah, E.; Low, H. T.; Kasiri-Asgarani, M.; Farahany, S.; Akbari, E.; Cho, M. H. Fabrication of biodegradable Zn-Al-Mg alloy: Mechanical properties, corrosion behavior, cytotoxicity and antibacterial activities. *Mater. Sci. Eng., C* **2017**, *73*, 215−219.

(49) Yang, H.; Wang, C.; Liu, C.; Chen, H.; Wu, Y.; Han, J.; Jia, Z.; Lin, W.; Zhang, D.; Li, W.; Yuan, W.; Guo, H.; Li, H.; Yang, G.; Kong, D.; Zhu, D.; Takashima, K.; Ruan, L.; Nie, J.; Li, X.; Zheng, Y. Evolution of the degradation mechanism of pure zinc stent in the one-year study of rabbit abdominal aorta model. *Biomaterials* **2017**, *145*, 92−105.

(50) Bowen, P. K.; Drelich, J.; Goldman, J. Zinc exhibits ideal physiological corrosion behavior for bioabsorbable stents. *Adv. Mater.* **2013**, *25* (18), 2577.

(51) Shen, Y.; Liu, W.; Wen, C.; Pan, H.; Wang, T.; Darvell, B. W.; Lu, W. W.; Huang, W. Bone regeneration: importance of local pH—strontium-doped borosilicate scaffold. *J. Mater. Chem.* **2012**, *22* (17), 8662−8670.

(52) Xiao, T.; Fan, L.; Liu, R.; Huang, X.; Wang, S.; Xiao, L.; Pang, Y.; Li, D.; Liu, J.; Min, Y. Fabrication of Dexamethasone-Loaded Dual-Metal-Organic Frameworks on Polyetheretherketone Implants with Bacteriostasis and Angiogenesis Properties for Promoting Bone Regeneration. *ACS Appl. Mater. Interfaces* **2021**, *13* (43), 50836−50850.

(53) Yamamoto, A.; Honma, R.; Sumita, M. Cytotoxicity evaluation of 43 metal salts using murine fibroblasts and osteoblastic cells. *J. Biomed. Mater. Res.* **1998**, *39* (2), 331−340.

(54) Wang, J.; Witte, F.; Xi, T.; Zheng, Y.; Yang, K.; Yang, Y.; Zhao, D.; Meng, J.; Li, Y.; Li, W.; Chan, K.; Qin, L. Recommendation for modifying current cytotoxicity testing standards for biodegradable magnesium-based materials. *Acta Biomater.* **2015**, *21*, 237−249.

(55) Tan, J.; Li, S.; Sun, C.; Bao, G.; Liu, M.; Jing, Z.; Fu, H.; Sun, Y.; Yang, Q.; Zheng, Y.; Wang, X.; Yang, H. A Dose-Dependent Spatiotemporal Response of Angiogenesis Elicited by Zn Biode-gradation During The Initial Stage of Bone Regeneration. *Adv. Healthcare Mater.* **2023**, 2302305.

(56) Rider, P.; Kačarević, Ž. P.; Elad, A.; Rothamel, D.; Sauer, G.; Bornert, F.; Windisch, P.; Hangyási, D.; Molnar, B.; Hesse, B.; Witte, F. Analysis of a Pure Magnesium Membrane Degradation Process and Its Functionality When Used in a Guided Bone Regeneration Model in Beagle Dogs. *Materials* **2022**, *15* (9), 3106.

(57) Si, J.; Shen, H.; Miao, H.; Tian, Y.; Huang, H.; Shi, J.; Yuan, G.; Shen, G. In vitro and in vivo evaluations of Mg-Zn-Gd alloy membrane on guided bone regeneration for rabbit calvarial defect. *J. Magnesium Alloys* **2021**, *9* (1), 281−291.

(58) Zhang, Z.; Jia, B.; Yang, H.; Han, Y.; Wu, Q.; Dai, K.; Zheng, Y. Zn0.8Li0.1Sr—a biodegradable metal with high mechanical strength comparable to pure Ti for the treatment of osteoporotic bone fractures: In vitro and in vivo studies. *Biomaterials* **2021**, *275*, 120905.

(59) Ewald, A.; Käppel, C.; Vorndran, E.; Moseke, C.; Gelinsky, M.; Gbureck, U. The effect of Cu(II)-loaded brushite scaffolds on growth and activity of osteoblastic cells. *J. Biomed. Mater. Res., Part A* **2012**, *100A* (9), 2392−2400.

(60) Wang, H.; Zhao, S.; Zhou, J.; Shen, Y.; Huang, W.; Zhang, C.; Rahaman, M. N.; Wang, D. Evaluation of borate bioactive glass scaffolds as a controlled delivery system for copper ions in stimulating osteogenesis and angiogenesis in bone healing. *J. Mater. Chem. B* **2014**, *2* (48), 8547−8557.

(61) Wang, Y.; Zhang, W.; Yao, Q. Copper-based biomaterials for bone and cartilage tissue engineering. *J. Orthop. Translat.* **2021**, *29*, 60−71.

(62) Zhuang, Y.; Liu, Q.; Jia, G.; Li, H.; Yuan, G.; Yu, H. A Biomimetic Zinc Alloy Scaffold Coated with Brushite for Enhanced Cranial Bone Regeneration. *ACS Biomater. Sci. Eng.* **2021**, *7* (3), 893−903.

(63) Shearier, E. R.; Bowen, P. K.; He, W.; Drelich, A.; Drelich, J.; Goldman, J.; Zhao, F. In Vitro Cytotoxicity, Adhesion, and Proliferation of Human Vascular Cells Exposed to Zinc. *ACS Biomater. Sci. Eng.* **2016**, *2* (4), 634−642.

(64) Santos, S. C.; Spaniol, K. G.; Chaves-Silva, N. E.; Fernandes, R. P. M.; Tavares, D. S.; Acchar, W.; dos Santos, E. A. Copper-containing bioactive glass/PVA membranes for guided bone regeneration. *J. Non-Cryst. Solids* **2021**, *557*, 120628.

(65) Foroutan, F.; McGuire, J.; Gupta, P.; Nikolaou, A.; Kyffin, B. A.; Kelly, N. L.; Hanna, J. V.; Gutierrez-Merino, J.; Knowles, J. C.; Baek, S.-Y.; Velliou, E.; Carta, D. Antibacterial Copper-Doped Calcium Phosphate Glasses for Bone Tissue Regeneration. *ACS Biomater. Sci. Eng.* **2019**, *5* (11), 6054−6062.

(66) Wu, C.; Zhou, Y.; Xu, M.; Han, P.; Chen, L.; Chang, J.; Xiao, Y. Copper-containing mesoporous bioactive glass scaffolds with multi-functional properties of angiogenesis capacity, osteostimulation and antibacterial activity. *Biomaterials* **2013**, *34* (2), 422−433.

(67) Lian, M.; Han, Y.; Sun, B.; Xu, L.; Wang, X.; Ni, B.; Jiang, W.; Qiao, Z.; Dai, K.; Zhang, X. A multifunctional electrowritten bi-layered scaffold for guided bone regeneration. *Acta Biomater.* **2020**, *118*, 83−99.

(68) Hu, H.; Tang, Y.; Pang, L.; Lin, C.; Huang, W.; Wang, D.; Jia, W. Angiogenesis and Full-Thickness Wound Healing Efficiency of a Copper-Doped Borate Bioactive Glass/Poly(lactic-co-glycolic acid) Dressing Loaded with Vitamin E in Vivo and in Vitro. *ACS Appl. Mater. Interfaces* **2018**, *10* (27), 22939−22950.

(69) Fan, Y.; Zhang, Y.; Zhao, Q.; Xie, Y.; Luo, R.; Yang, P.; Weng, Y. Immobilization of nano Cu-MOFs with polydopamine coating for adaptable gasotransmitter generation and copper ion delivery on cardiovascular stents. *Biomaterials* **2019**, *204*, 36−45.

(70) Xiang, E.; Gómez-Cerezo, M. N.; Ali, Y.; Ramachandra, S. S.; Yang, N.; Dargusch, M.; Moran, C. S.; Ivanovski, S.; Abdal-hay, A. Surface Modification of Pure Zinc by Acid Etching: Accelerating the Corrosion Rate and Enhancing Biocompatibility and Antibacterial Characteristics. *ACS Appl. Mater. Interfaces* **2022**, *14* (19), 22554−22569.

(71) Gao, Y.; Hao, Y.; Zhang, W.; Wei, Y.; Shu, Y.; Wang, J. Microwave-triggered ionic liquid-based hydrogel dressing with excellent hyperthermia and transdermal drug delivery performance. *Chem. Eng. J.* **2022**, *429*, 131590.

(72) Shuai, C.; Dong, Z.; He, C.; Yang, W.; Peng, S.; Yang, Y.; Qi, F. A peritectic phase refines the microstructure and enhances Zn implants. *J. Mater. Res. Technol.* **2020**, *9* (3), 2623−2634.

(73) Zhang, E.; Zhao, X.; Hu, J.; Wang, R.; Fu, S.; Qin, G. Antibacterial metals and alloys for potential biomedical implants. *Bioact. Mater.* **2021**, *6* (8), 2569−2612.

(74) Li, M.; Ma, Z.; Zhu, Y.; Xia, H.; Yao, M.; Chu, X.; Wang, X.; Yang, K.; Yang, M.; Zhang, Y.; Mao, C. Toward a Molecular Understanding of the Antibacterial Mechanism of Copper-Bearing Titanium Alloys against Staphylococcus aureus. *Adv. Healthcare Mater.* **2016**, *5* (5), 557−566.

(75) Tan, J.; Wang, D.; Cao, H.; Qiao, Y.; Zhu, H.; Liu, X. Effect of Local Alkaline Microenvironment on the Behaviors of Bacteria and Osteogenic Cells. *ACS Appl. Mater. Interfaces* **2018**, *10* (49), 42018−42029.